Chemical Geology 343 (2013) 38–54

Contents lists available at SciVerse ScienceDirect

Chemical Geology

journal homepage: www.elsevier.com/locate/chemgeo

High-pressure serpentinites, a trap-and-release system controlled by metamorphic conditions: Example from the Piedmont zone of the western Alps

Romain Lafay [a,*], Fabien Deschamps [b], Stéphane Schwartz [a], Stéphane Guillot [a], Marguerite Godard [b], Baptiste Debret [c], Christian Nicollet [c]

[a] ISTerre, Université Grenoble I, CNRS 1381 rue de la Piscine, 38400 Grenoble Cedex 09, France
[b] Géosciences Montpellier, Université Montpellier 2, CNRS, cc60, Place E. Bataillon, 34095 Montpellier, France
[c] Laboratoire Magmas and Volcans, Université Blaise Pascal, CNRS, F-63038 Clermont-Ferrand Cedex, France

ARTICLE INFO

Article history:
Received 21 February 2012
Received in revised form 8 February 2013
Accepted 10 February 2013
Available online 18 February 2013

Editor: L. Reisberg

Keywords:
Serpentinization
Accretionary wedge
Fluid-mobile elements
Trap-and-release system

ABSTRACT

We provide new insights into the geochemistry of serpentinites from the Alpine orogenic wedge representing a paleo-subduction zone. These serpentinites are derived from similar oceanic protoliths, but they have experienced different metamorphic conditions related to three different structural levels of the paleo-subduction zone ((1) obducted: Chenaillet ophiolite, (2) accretionary wedge: Queyras Schistes lustrés complex and (3) serpentinite channel: Monviso ophiolite). Metamorphism undergone by these three units is well defined, increasing eastward from sub-greenschist to eclogite facies conditions, and allows us to examine trace element behavior from the oceanic ridge environment to subduction. Serpentinites first record moderate trace element enrichment due to seawater interaction resulting in the replacement of olivine and pyroxene by chrysotile and lizardite below 300 °C. In the sediment-dominated accretionary wedge, serpentinites are strongly enriched in fluid-mobile-elements (B, Li, As, Sb, and Cs) and act as a trapping system following the metamorphic gradient (from 300 to 390 °C) up to total replacement of the lizardite/chrysotile assemblage by antigorite. Under higher temperature conditions (T > 390 °C), no enrichment was observed, and some fluid-mobile elements were released (B, Li, Cs, and Sr). Moreover, in the serpentinite channel (T > 460 °C), most of the fluid-mobile elements are absent due to the scarcity of metasediments which prevent geochemical exchange between metasediments and serpentinites. This is also due to the onset of antigorite breakdown and the release of fluid-mobile elements. Thus, we emphasize that the geochemistry of Alpine serpentinites is strongly dependent on (1) the grade of metamorphism and (2) the ability of metasediments to supply fluid-mobile elements. We conclude that serpentinites act as a trap-and-release system for fluid-mobile elements in a subduction context.

1. Introduction

Serpentinites are recognized as an important pathway for water transport in settings ranging from oceanic spreading ridges to subduction zones and thus play an important role in the global geochemical cycle (Ulmer and Trommsdorff, 1995; Scambelluri et al., 2001; Rüpke et al., 2002; Hattori and Guillot, 2003, 2007; Deschamps et al., 2010). Serpentinites formed in abyssal environment which incude the serpentine species (lizardite (Lz), chrysotile (Ctl), and antigorite (Atg)) are characterized by strong enrichment in fluid-mobile elements (Thompson and Melson, 1970; Seitz and Hart, 1973; Moody, 1976; Bonatti et al., 1984; Deschamps et al., 2011, 2012; Pabst et al., 2011; Kodolányi et al., 2012), which are mainly due to fluid/rock interactions and hydrothermal activity occurring in slow-spreading ridge environments. During subduction, serpentinites undergo dehydration at roughly 650–700 °C (the so-called "*antigorite breakdown*", Ulmer and Trommsdorff, 1995; Wunder and Schreyer, 1997) allowing the release of water and fluid-mobile elements through the mantle wedge (Scambelluri and Philippot, 2001; Scambelluri et al., 2001, 2004; Hattori and Guillot, 2003; Deschamps et al., 2010; Kodolányi and Pettke, 2011; Vils et al., 2011). These fluids transported into the mantle wedge can contribute to the formation of arc magmas (Hattori and Guillot, 2003, 2007) and partly control their geochemical signatures. Recently, Deschamps et al. (2011) used Pb isotopes to show that over-enrichment in fluid-mobile elements in serpentinites can be related to early sediment dehydration during subduction. The timing and the modality of this geochemical exchange between serpentinites and metasediments remain unclear.

* Corresponding author.
E-mail address: romain.lafay@ujf-grenoble.fr (R. Lafay).

0009-2541/$ – see front matter © 2013 Elsevier B.V. All rights reserved.
http://dx.doi.org/10.1016/j.chemgeo.2013.02.008

In the western Alps, the Piedmont zone corresponds to the juxtaposition of different levels of a paleo-subduction zone. From the top to the bottom, we observe the following: (i) the obducted Chenaillet ophiolite; (ii) the Schistes lustrés complex dominated by oceanic sediments; and (iii) the Monviso ophiolite composed of mafic-to-ultramafic rocks related to the deeply subducted oceanic lithosphere. The present-day geometry corresponds to an orogenic wedge tilted to the west. The metamorphic P–T conditions increase eastward from sub-greenschist facies conditions to eclogite facies conditions (Goffé et al., 2004).

Sampling these different levels of the paleo-subduction zone offers the unique opportunity to trace the changes in the chemical composition of serpentinites along a low-temperature metamorphic gradient related to subduction dynamics. In this study, we present whole rock chemical analyses of serpentinites and associated sediments, as well as in situ analyses by laser ablation (LA) coupled with inductively coupled plasma (ICP) mass spectrometry (MS) (LA-ICP-MS) of serpentines. This approach allows: (i) tracing the geochemical evolution of serpentinites; (ii) constraining major and trace element behavior in relation to the structural level of the paleo-subduction zone; and (iii) deciphering the fluid exchange between serpentinites and metasediments during subduction processes.

2. Geological setting

The Piedmont zone of the internal part of the Western Alps (Fig. 1a) was formed by the juxtaposition of continental and oceanic units derived from the distal European margin and the oceanic domain (Lemoine et al., 1986). These units result from the closure of the Ligurian ocean, a part of the Tethys ocean, which occurred from the Late Cretaceous to the Oligocene (Handy et al., 2010). They represent a paleo-subduction zone deformed and metamorphosed under high-pressure and low-temperature conditions (HP-LT) during subduction from Northwest to Southeast. This paleo-subduction complex was exhumed and deformed during the Oligocene collision (Agard et al., 2002; Lardeaux et al., 2006; Tricart and Schwartz, 2006; Schwartz et al., 2009). The Piedmont zone is composed by the association of sediment, mafic and ultramafic lithologies related to the Tethyan oceanic lithosphere. From North to South the following units are outcropping in the piedmont zone: the Chenaillet ophiolite, the Schistes lustrés complex and the Monviso ophiolite. The Chenaillet ophiolite escaped high-pressure and low-temperature (HP-LT) metamorphism and represents a piece of the Tethyan ocean. Presently, the Chenaillet ophiolite lies on the Schistes lustrés complex. The Schistes lustrés complex corresponds to the sedimentary accretionary wedge derived from oceanic sediments (Lemoine et al., 1984). This complex is composed of a west-dipping, ten-kilometer thick nappe stack. Series within the Schistes lustrés complex are composed by heterogeneous metasediments (metamorphic marls, clays, and limestones) enclosing decametric-to-kilometric lenses of oceanic rocks (basalt, gabbro, serpentinite) (Tricart and Lemoine, 1991; Schwartz et al., 2009). The Schistes lustrés complex records blueschist facies conditions (Goffé et al., 2004) and was exhumed and tilted toward the west, generating extensional brittle structures during the Neogene (Tricart et al., 2004). The Monviso ophiolite is mainly composed of mafic and ultramafic rocks originating from the oceanic lithosphere that were strongly deformed and metamorphosed under eclogitic-facies conditions (Lombardo et al., 1978; Schwartz et al., 2000; Angiboust et al., 2011).

Previous studies (Agard et al., 2001; Goffé et al., 2004; Tricart and Schwartz, 2006; Schwartz et al., 2007, 2009; Angiboust et al., 2011) have identified several metamorphic units in the Piedmont zone (Fig. 1b). In this study, six metamorphic Grades have been defined. The Chenaillet ophiolite has recorded sub-greenschist-facies conditions ($200<T<300$ °C; $P<4$ kbar) and corresponds to Grade 0. In the Schistes lustrés complex, four Grades are distinguished, which record an increase of the P–T conditions eastward. In detail, the westward domain presents low-temperature blueschist-facies conditions ($300<T<350$ °C; $9<P<11$ kbar), this domain corresponds to Grade 1. The central domain records medium-temperature blueschist facies conditions, and it is divided into Grade 2 ($340<T<360$ °C; $10<P<12$ kbar) and Grade 3 ($360<T<390$ °C; $10<P<12$ kbar). The eastward domain has recorded high-temperature blueschist facies conditions ($390<T<480$ °C; $P>12$ kbar) and corresponds to Grade 4. In the Monviso ophiolite, all metamorphic assemblages are eclogitic ($T>460$ °C, $P>20$ kbar) and correspond to Grade 5.

In these six metamorphic grade domains, we collected a total of 18 samples including serpentinites and metasediments to investigate the geochemical evolution of serpentinites in each level of the paleo-subduction zone associated with the paleo-thermal gradient recorded during the subduction (Fig. 1b and c; Table 1).

3. Sample description

Eight metasediments (Fig. 1b) were collected, in a west–east transect, in Cretaceous calcareous-schists (Lemoine et al., 1984) derived from foraminifera oozes. Metasediments show lithologic variability owing to different clay versus carbonate fractions in their protoliths. The carbonate contents result from both biogenic production (pelagic foraminifera) and from detrital input (calciturbidites). Due to this high lithological heterogeneity, it is difficult to sample a single lithology all along the transect. The samples are strongly deformed, and the main schistosity is dominated by phengite, quartz, calcite and oxides. Glaucophane and pseudomorphs of lawsonite or zoisite are also present. In the Chenaillet ophiolite, the only sedimentary component corresponds to ophicalcite sediments. Because these sediments have a hydrothermal origin (Lemoine et al., 1983), we do not use them in this study.

Ten serpentinites were sampled from the studied area. Two come from Chenaillet ophiolite, four come from the Schistes lustrés complex and four come from the Monviso eclogitic unit (Fig. 1). These samples were systematically collected in preserved zones in the absence of retrogressed mineral phases. The serpentine mineral identification is described in detail in a companion paper (Schwartz et al., 2013) and was performed using optical and Raman spectroscopy (Table 1). All the serpentinites (Fig. 1b) display morphological oceanic features serpentinites with pseudomorphic textures (Wicks and Whittaker, 1977; Mével, 2003) (Fig. 2). These textures are the result of the remplacement of the primary assemblage (dominated by pyroxene and olivine) by serpentine. The replacement of olivine induces the formation of a mesh texture due to multiple hierarchic micro-fractures and formation of sub-grains. The replacement of pyroxene minerals during hydration of the oceanic lithosphere by oceanic water circulation induces the formation of bastite. The general serpentinization reaction can be expressed as: olivine + enstatite + H_2O = serpentine + magnetite ± brucite (Martin and Fyfe, 1970; Seyfried et al., 2007). Note that in all our samples no brucite was identified. The absence of brucite could be interpreted as the result of a lower degree of olivine hydration with respect to enstatite hydration precluding any release of Mg necessary for the brucite crystallization or alternatively that brucite is consumed during prograde reactions. Lizardite is the dominant phase in serpentinites and replaces the primary olivine and pyroxene, whereas chrysotile is present in veins cross-cutting the mesh

Fig. 1. (a) Tectonic sketch map of the western Alps. (b) Simplified geological map of the studied area located in the Schistes lustrés complex of the Piedmont zone (modified from Schwartz et al., 2013). This domain is bounded by the Briançonnais zone to the west and by the internal crystalline massif of Dora Maira to the east. The Schistes lustrés complex corresponds to a calcschist-rich accretionary wedge enclosing scattered ophiolitic bodies metamorphosed under HP facies conditions. Ten serpentinites and eight metasediments have been sampled from sub-greenschist (Chenaillet) to eclogitic (Monviso) facies conditions. Sample locations are indicated by black stars.

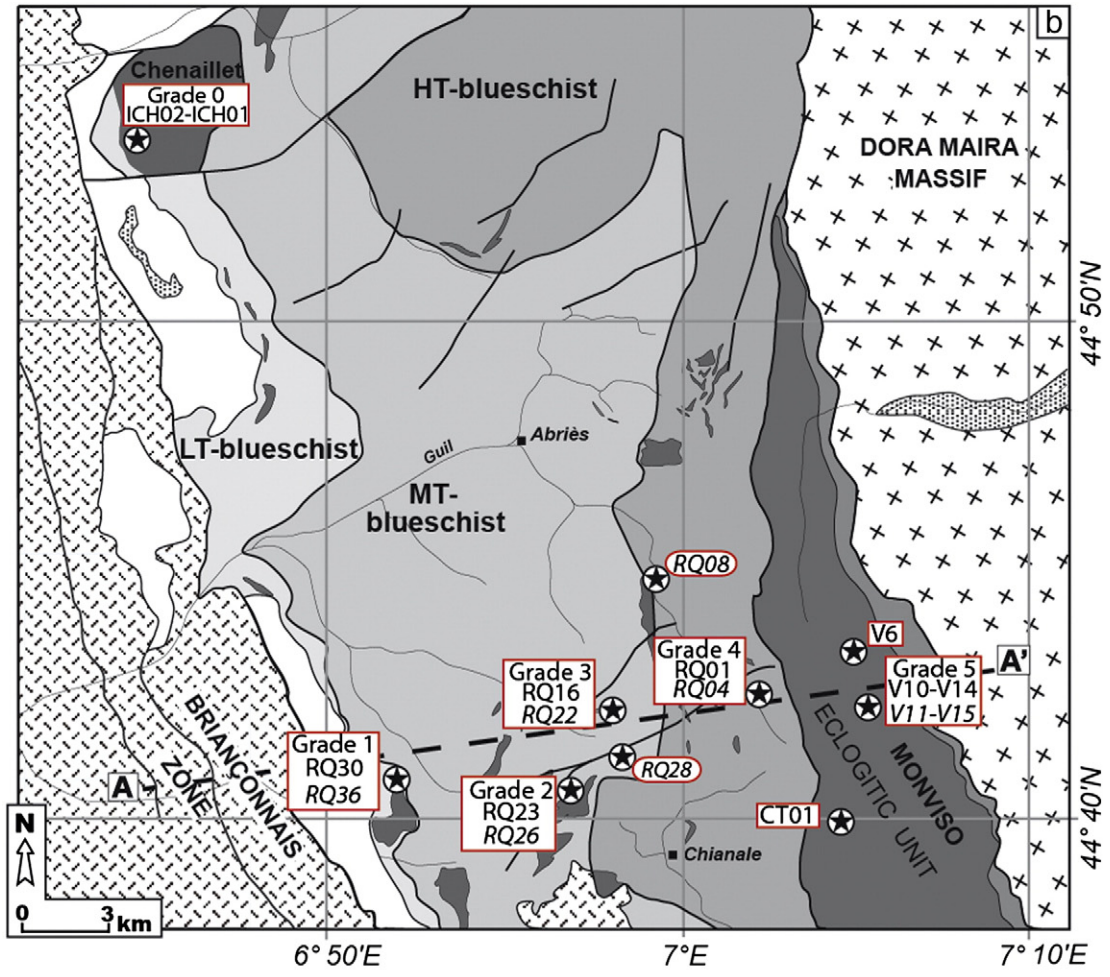
b
Chenaillet
Grade 0
ICH02-ICH01
HT-blueschist
DORA MAIRA
MASSIF
LT-blueschist
Guil
Abriès
MT-
blueschist
RQ08
V6
Grade 4
RQ01
RQ04
Grade 5
V10-V14
V11-V15
A'
Grade 3
RQ16
RQ22
BRIANÇONNAIS
ZONE
ECLOGITIC
UNIT
MONVISO
Grade 1
RQ30
RQ36
RQ28
A
Grade 2
RQ23
RQ26
CT01
Chianale
N
0
3 km
44° 50'N
44° 40'N
6° 50'E
7°E
7° 10'E

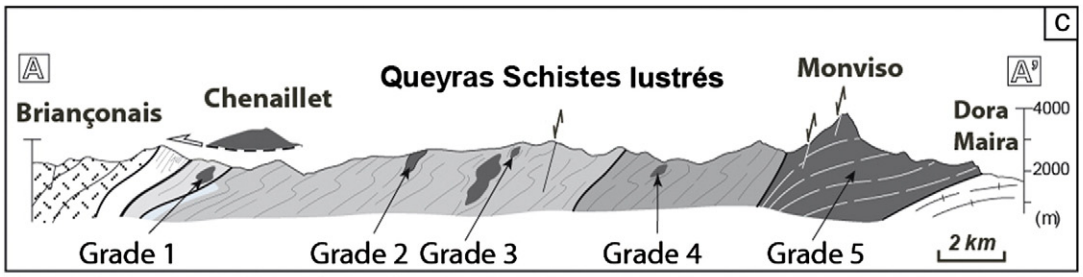
c
A
Briançonais
Chenaillet
Queyras Schistes lustrés
Monviso
A'
Dora
Maira
4000
2000
(m)
Grade 1
Grade 2
Grade 3
Grade 4
Grade 5
2 km

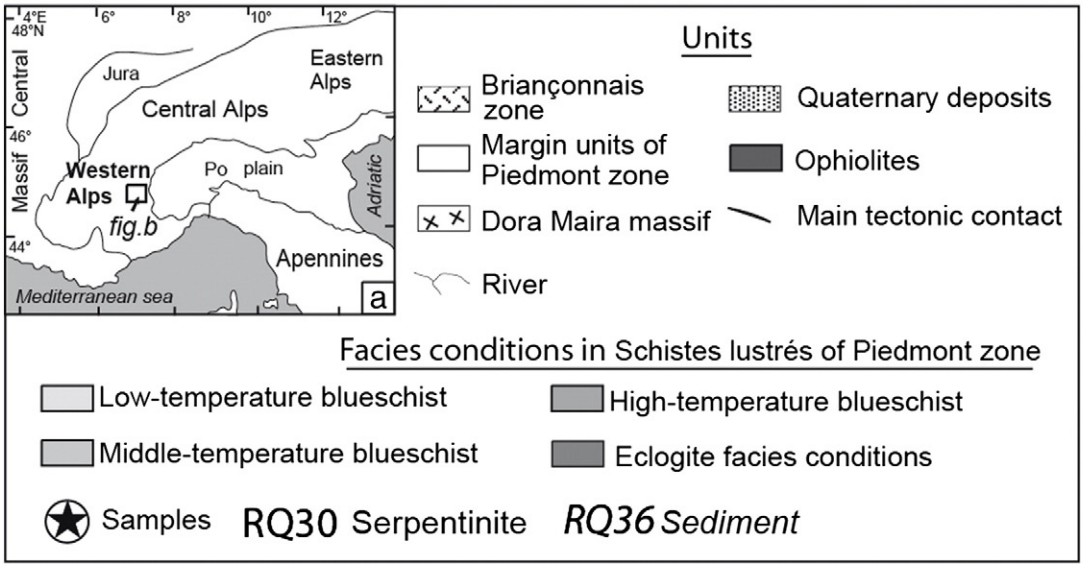
4°E
48°N
6°
8°
10°
12°
Central
Massif
46°
44°
Jura
Eastern
Alps
Central Alps
Western
Alps
fig.b
Po plain
Adriatic
Apennines
Mediterranean sea
a
Units
Briançonnais
zone
Quaternary deposits
Margin units of
Piedmont zone
Ophiolites
Dora Maira massif
Main tectonic contact
River
Facies conditions in Schistes lustrés of Piedmont zone
Low-temperature blueschist
High-temperature blueschist
Middle-temperature blueschist
Eclogite facies conditions
Samples
RQ30 Serpentinite
RQ36 Sediment

Table 1
Locations, metamorphic conditions and nature of serpentine phases for samples (serpentinites and metasediments) analyzed in this study. Data come from Schwartz et al., 2013.

Serpentinites	Sediments	Location	T (°C)	P (Kbar)	Metamorphic grade	Serpentine phases				Secondary phases
						Lz.	Ctl.	mixed	Atg.	
ICH01–ICH02	(*none*)	Chenaillet	200–300	<4	0	+++	+	−	−	relictual cpx; mt
RQ30	RQ36	Rocher Blanc	300–350	9–11	1	++	++	−	+	relictual cpx; mt
RQ23	RQ26–RQ28	Rocca Bianca	340–360	10–12	2	++	−	++	++	mt
RQ16	RQ22	Eychassier	360–390	10–12	3	+	-	++	++	mt
RQ01	RQ04–RQ08	Refuge du Viso	390–480	12–15	4	−	−	−	+++	mt
V6–CT01 V14–V10	V11–V15	Viso	>480	>20	5	−	−	−	+++	mt; chl; ol

cpx: clinopyroxene, mt: magnetite, chl: chlorite, ol: olivine.

texture. Magnetite is occurs as submillimetric veins surrounding mesh and bastite. A clear identification of serpentinite mineral texture provides important information on the nature of the initial peridotite.

Serpentinites ICH01 and ICH02 from Chenaillet (Grade 0) are not deformed, and their original texture is preserved (pseudomorphic texture), with fresh primary pyroxenes and olivines still visible. The samples are mainly dominated by lizardite, showing mesh and replacing, principally, primary olivine due to the circulation of hydrothermal fluids in an abyssal environment. Chrysotile veins crosscut the texture; they may be related to early fluids circulating during oceanic serpentinization (Andréani et al., 2007) and/or during obduction process (Fig. 2a). Because Chenaillet ophiolite and related serpentinites were obducted during Alpine history, they can be used as a reference for comparison with other serpentinite samples.

Serpentinites from the Schistes lustrés complex were collected in hectometric-to-kilometric lenses of ultramafic rock enclosed in metasediments. All serpentinites were sampled in undeformed zones where the pseudomorphic texture is preserved. From West to East, we sampled different serpentinite lenses (Fig. 1b): the Rocher Blanc (RQ30) corresponding to Grade 1, the Rocca Bianca (RQ23) corresponding to Grade 2, the Eychassier (RQ16) corresponding to Grade 3 and the Refuge du Viso (RQ01) corresponding to Grade 4 (Table 1). Serpentinites from Grade 0 to Grade 3 are dominated by low-grade serpentine phases (lizardite and chrysotile). The amount of antigorite increases in surface, optically, from Grade 1 (<10%) to Grade 3 (>50%). Antigorite grows, at the expense of lizardite, along grain boundaries producing antigorite vein networks (Fig. 2b). In Grades 2 and 3, lizardite preserved in mesh texture systematically shows an intermediate Raman spectrum between lizardite and antigorite and is interpreted as a mixed antigorite/lizardite serpentine related to the destabilization of lizardite to antigorite at the core of the mesh texture (Fig. 2b). In sample RQ23 (Grade 2), we observed local antigorite patches superimposed on the mesh texture (Fig. 2c). Serpentinites from Grade 4 and Grade 5 samples are mainly composed of antigorite, in both mesh texture and bastite, without any evidence of the mixed antigorite/lizardite serpentine. Samples from the eclogitic unit of the Monviso ophiolite (CT01-V6-V10-V14) corresponding to Grade 5 are slightly deformed, but exhibit a locally preserved oceanic-type pseudomorphic texture (Fig. 2d). Locally, chlorite and metamorphic olivine crystallized at the expense of antigorite. This has been demonstrated by X-ray powder diffraction (XRD) measurements (Schwartz et al., 2013) and is indicative of the onset of deserpentinization (e.g., Scambelluri and Philippot, 2001; Scambelluri et al., 2001, 2004; Evans, 2004). Chemical formulas, textural characteristics and P–T stability fields of the three types of serpentine are presented in Table 2.

4. Analytical techniques

4.1. Whole rock major and trace element compositions

Part of each sample was crushed and reduced to powder in an agate ring mill for further whole rock measurements. Major element concentrations were analyzed by Inductively Coupled Plasma Emission Spectrometry (Thermo ICP-OES Icap 6500) at the "Service d' Analyse des Roches et des Minéraux" at "Centre de Recherches Pétrographiques and Géochimiques" (CRPG), Nancy, France. Analytical procedures and uncertainties are described in detail in Carignan et al., 2001. Data are reported in Table 3. The precision and accuracy is better than 1% for >10 wt.% oxide proportion, within 1–5% for 1–5 wt.% oxide proportion and 5–15% for >0.5 wt.% oxide proportion.

Trace element concentrations (Li, Cd, Co, Ni, Cu, As, Rb, Sr, Y, Zr, Nb, Cs, Ba, rare earth elements (REE), Hf, Ta, Pb, Th, U and W) were determined at Géosciences Montpellier (Université Montpellier 2, France) using an Agilent 7700X quadrupole ICP-MS. The analytical procedure is described by Ionov et al. (1992) and Godard et al. (2000). The precision and accuracy of the analyses were assessed by measuring four rock standards as unknowns: peridotite JP-1, serpentinite UBN, basalt BEN, and shale OU-6 (values are presented in the Appendix 1). Precision is generally better than 1% at concentrations >1 μg/g; it is within 1–5% for concentrations of 10–1000 ng/g, and 5–10% for concentrations less than 10 ng/g. Measured values for most of the elements are comparable with expected values from the international standards. Table 3 presents the results of the trace elements analyses for serpentinites and metasediments. We observed a bias compare to reference values for As, Li, Mo, U and W (25–40%), and for Ni, Cu, Rb, Sr, Y, Zr, La, Pr, Nd, Tb, Dy, Er, Hf (10–21%) (see Appendix 1). The offset is under 10% for all the other elements. Despite these systematic biases, the reproducibility of each standard is good for all elements except Li, U and Th. In addition, whole rock trace element data for our samples display significant chemical trends. Thus in this study we do not insist on the absolute element values but instead discuss our results in terms of global trends relative to those of in-situ measurements.

4.2. Mineral geochemistry

Major element concentrations were determined using a Cameca SX 100 electron-microprobe at the "Laboratoire Magma et Volcans" (Clermont Ferrand University, France). Operating conditions of 15 kV accelerating voltage, a sample current of 15 nA and a counting time of 10 s/element were used, except for Ni (20 s). Standards used were albite (Na), forsterite (Mg and Ni), orthose (K), wollastonite (Ca

Fig. 2. Thin-section photomicrographs of serpentinites (left: normal light; right: cross polarized light). (a) Sample ICH02 (Grade 0) with lizardite (lz) forming pseudomorphic texture (mesh with hourglass texture after olivine). Magnetite (mt) is located at the rim of primary olivines. Secondary veins are filled with chrysotile (ctl). (b) Sample RQ30 (Grade 2) with mesh and bastite (bs) textures dominate by lizardite and chrysotile assemblage (c) Sample RQ16 (Grade 3) with pseudomorphic texture (mixed serpentine). Note the appearance of antigorite (atg) at the expense of grain boundary. (d) Sample RQ23 (Grade 2), mesh texture characterized by lizardite/mixed varieties and antigorite patches. (e) Sample CT01 (Grade 5), pseudomorphic texture fully replaced by antigorite, and focus on chlorite (chl) and metamorphic olivine (ol) replacing antigorite in a deformed area.

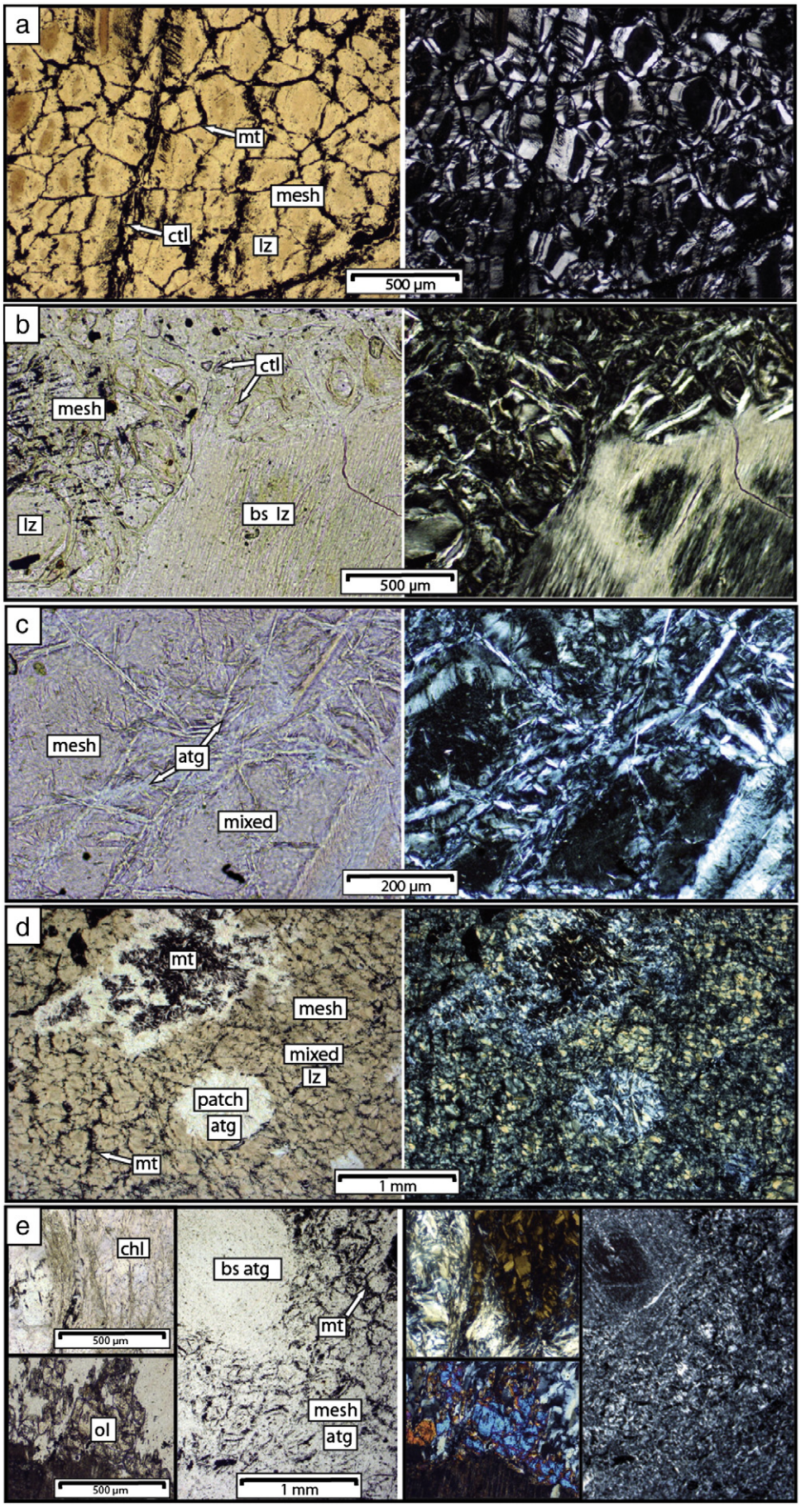
a
mt
mesh
ctl
lz
500 µm
b
ctl
mesh
lz
bs lz
500 µm
c
mesh
atg
mixed
200 µm
d
mt
mesh
mixed
lz
patch
atg
mt
1 mm
e
chl
500 µm
bs atg
mt
ol
500 µm
mesh
atg
1 mm

Table 2
Chemical formulas, temperature stability fields and general textural characteristics of different serpentine varieties (modified after Evans, 2004).

Variety	Formula	Temp. (°C) stability range	Origin and texture
Chrysotile	$Mg_3Si_2O_5(OH)_4$	50–300	Veins and replacements
Lizardite	$Mg_3Si_2O_5(OH)_4$	0–400	Hydration of peridotite (mesh/bastite)
Antigorite	$Mg_{48}Si_{34}O_{85}(OH)_{62}$	300–650	Recryst. of serp. Hydrat. of peridotite (mesh/bastite)

and Si), $MnTiO_3$ (Ti and Mn), Cr_2O_3 (Cr), fayalite (Fe) and synthetic Al_2O_3 (Al).

In situ trace element compositions were determined at "Géosciences Montpellier" (Montpellier 2 University, France) using a ThermoFinnigan Element 2 HR-ICP-MS with a single collector double-focusing sector field Element XR (eXtended Range) coupled with a laser ablation system, a Geolas (Microlas) automated platform housing a 193 nm Compex 102 laser from LambdaPhysik. Analyses were performed on 150 μm thick polished sections in a modified ablation cell of 30 cm^3, which results in a shorter washout time and an improved sensitivity compared to the initial, larger ablation cell. To enhance sensitivity and reduce inter-element fractionation, ablation experiments were conducted in a helium atmosphere (Gunther and Heinrich, 1999). The helium gas and particles from the sample were then mixed with argon before entering the plasma. Time resolved Signals were acquired in time-resolved acquisition, devoting 2 min to the blank and 1 min to the measurement of the samples. The laser was fired using an energy density of 15 Jcm^{-2} at a frequency of 7 Hz and a spot size of 102 μm. This large beam size was used during this study to obtain a higher sensitivity and a higher measurement precision. This resulted in a sensitivity of ~1000 cps/μg/g for B, ~1200 cps/μg/g for As, ~2200 cps/μg/g for Li, ~4100 cps/μg/g for Sb, ~15,000 cps/μg/g for Cs. The sensitivity of other trace and minor

Table 3
Whole rock major (ICP-OES; wt.%) and trace element (ICP-MS; μg/g) concentrations for serpentinites and metasediments (b.d.l.: below detection limit; n.d.: not determined).

	Serpentinite								Sediments							
Sample	ICH01	ICH02	RQ30	RQ23	RQ16	RQ01	V14	V10	RQ36	RQ26	RQ28	RQ22	RQ04	RQ08	V11	V15
Grade	0	0	1	2	3	4	5	5	1	2	2	3	4	4	5	5
SiO_2	39.3	39.6	38.6	39.9	40.0	40.1	40.4	40.7	67.4	48.7	50.8	39.6	26.8	38.4	57.2	48.2
Al_2O_3	1.6	1.0	1.6	0.7	2.3	1.3	1.5	1.4	14.2	19.5	18.4	11.0	8.4	11.3	10.6	17.3
Fe_2O_3	8.4	7.8	9.0	9.4	8.0	7.6	7.8	8.1	7.0	7.0	6.5	4.5	3.6	6.3	5.5	7.1
MnO	0.09	0.09	0.08	0.08	0.11	0.12	0.11	0.09	0.30	0.10	0.19	0.18	0.08	0.24	0.18	0.15
MgO	36.1	37.9	37.0	36.5	35.4	37.9	37.4	37.4	2.8	2.6	2.5	1.9	1.7	2.4	3.5	2.2
CaO	0.77	0.05	0.04	b.d.l.	0.11	0.21	b.d.l.	b.d.l.	0.2	6.2	6.6	19.6	30.8	19.3	10.1	9.8
Na_2O	b.d.l.	b.d.l.	b.d.l.	b.d.l.	b.d.l.	b.d.l.	b.d.l.	b.d.l.	0.86	0.93	1.40	3.81	0.22	0.81	0.79	0.81
K_2O	b.d.l.	b.d.l.	b.d.l.	b.d.l.	b.d.l.	b.d.l.	b.d.l.	b.d.l.	2.13	4.14	2.99	1.10	1.76	1.42	1.62	3.21
TiO_2	0.05	0.02	0.02	0.03	0.08	0.01	0.03	0.02	0.53	0.89	0.83	0.49	0.37	0.61	0.51	0.78
P_2O_5	b.d.l.	b.d.l.	b.d.l.	b.d.l.	b.d.l.	b.d.l.	b.d.l.	b.d.l.	0.09	0.14	0.12	0.08	0.09	0.10	0.11	0.13
L.O.I.	12.4	13.2	12.9	12.1	12.6	11.9	11.8	11.6	3.7	8.8	9.0	17.1	26.3	18.5	9.4	10.8
Total	98.7	99.6	99.1	98.8	98.7	99.1	99.0	99.3	99.2	99.0	99.4	99.3	100.2	99.3	99.6	100.4
Li	0.29	0.27	2.11	0.48	4.01	0.05	0.20	0.18	53.1	35.8	63.3	10.8	16.6	35.7	9.7	18.6
Co	87.7	93.6	93.6	98.0	91.7	82.9	89.3	87.5	22.3	15.1	25.2	12.0	9.4	12.4	32.7	24.0
Ni	1692	1811	1819	2021	1824	1083	1826	1749	97.5	58.5	90.6	39.9	35.4	35.0	141.9	70.3
Cu	12.2	28.0	14.4	43.4	24.8	6.6	27.7	1.0	41.2	39.5	73.9	30.4	24.5	26.3	64.7	44.4
Zn	36.7	146.3	37.0	56.7	139.6	44.9	55.2	45.2	100.6	110.2	161.3	72.6	58.9	74.6	76.6	167.2
As	0.05	0.22	0.14	0.90	0.52	3.97	0.90	0.44	2.68	5.29	9.49	3.68	3.19	3.38	3.48	6.92
Mo	0.020	0.032	0.028	0.025	0.015	0.025	0.027	0.019	0.10	0.44	1.29	0.59	0.78	0.28	0.15	0.83
Sb	0.004	0.028	0.014	0.129	0.238	0.995	0.049	0.029	0.16	0.44	1.26	0.17	0.23	0.25	0.20	0.33
W	0.015	n.d.	n.d.	0.021	n.d.	0.042	n.d.	n.d.	1.51	1.29	2.36	0.92	0.75	1.52	0.38	1.71
Rb	0.12	0.11	0.15	0.20	0.65	0.07	0.25	0.11	84.7	162.4	159.3	39.9	65.4	64.9	81.9	157.4
Sr	1.78	1.34	4.61	2.04	5.70	0.30	0.43	0.25	20.2	142.6	222.5	496.5	364.8	415.7	148.3	148.9
Y	1.27	0.36	1.30	0.57	3.22	0.49	1.18	0.79	10.0	17.6	24.0	20.9	18.2	16.7	26.4	28.3
Zr	0.50	0.69	0.40	1.25	1.55	0.07	0.41	0.24	75.8	86.2	134.9	40.6	19.2	61.3	18.6	26.1
Nb	0.010	0.016	0.011	0.023	0.022	0.012	0.056	0.049	10.6	16.5	25.2	9.8	7.5	13.4	11.4	20.2
Cs	0.01	0.01	0.25	0.65	3.03	0.01	0.03	0.01	5.2	8.0	10.4	2.1	3.2	3.8	2.7	6.7
Ba	1.30	7.14	3.02	1.09	5.70	0.90	2.76	1.10	226.4	394.3	424.1	150.8	190.2	126.6	90.8	362.6
La	0.015	0.058	0.036	0.103	0.102	0.056	0.224	0.078	20.5	40.3	55.9	25.5	18.2	26.8	27.9	43.3
Ce	0.037	0.127	0.127	0.208	0.280	0.130	0.591	0.216	47.4	80.3	110.3	51.1	33.7	52.9	62.4	87.9
Pr	0.007	0.016	0.025	0.028	0.056	0.014	0.079	0.034	4.87	8.89	12.09	5.61	4.01	5.92	6.54	9.45
Nd	0.066	0.088	0.157	0.134	0.355	0.063	0.381	0.174	19.8	34.7	46.9	22.0	15.9	24.2	26.5	36.7
Sm	0.045	0.038	0.062	0.038	0.156	0.016	0.096	0.054	3.48	6.06	8.20	3.98	2.97	5.40	5.16	6.64
Eu	0.022	0.019	0.026	0.026	0.060	0.008	0.032	0.021	0.66	1.46	1.57	0.97	0.75	1.61	1.29	1.67
Gd	0.103	0.056	0.116	0.056	0.295	0.035	0.140	0.088	3.00	6.25	8.19	4.44	3.44	6.11	5.94	7.23
Tb	0.021	0.008	0.023	0.010	0.057	0.008	0.023	0.015	0.33	0.74	1.02	0.59	0.46	0.76	0.82	0.96
Dy	0.177	0.055	0.175	0.073	0.443	0.069	0.168	0.111	1.71	3.92	5.32	3.42	2.74	3.85	4.92	5.60
Ho	0.041	0.011	0.041	0.017	0.101	0.017	0.038	0.026	0.34	0.72	0.94	0.65	0.54	0.65	0.97	1.08
Er	0.128	0.031	0.125	0.054	0.300	0.056	0.109	0.079	1.00	1.99	2.53	1.75	1.47	1.69	2.64	2.98
Tm	0.020	0.005	0.019	0.009	0.045	0.009	0.017	0.013	0.15	0.28	0.34	0.23	0.20	0.23	0.36	0.41
Yb	0.144	0.034	0.132	0.074	0.307	0.071	0.120	0.093	1.16	2.01	2.26	1.39	1.26	1.53	2.30	2.57
Lu	0.025	0.006	0.025	0.015	0.053	0.012	0.021	0.016	0.19	0.32	0.38	0.21	0.18	0.25	0.34	0.38
Hf	0.043	0.033	0.019	0.039	0.100	0.006	0.021	0.016	2.19	2.29	2.44	1.23	0.56	1.33	0.49	0.62
Ta	b.d.l	b.d.l	b.d.l	0.002	b.d.l	b.d.l	0.003	0.003	0.82	1.08	1.55	0.74	0.56	0.61	0.72	1.01
Pb	n.d.	4.99	n.d.	1.54	5.88	1.07	2.24	1.01	10.80	14.28	23.81	12.25	18.68	14.68	9.72	45.09
Th	0.007	0.011	b.d.l	0.005	0.007	0.014	0.024	0.011	7.43	11.83	14.35	6.88	4.97	7.66	7.81	12.25
U	0.001	0.009	n.d.	0.004	0.003	0.003	0.034	0.065	0.99	1.58	2.09	1.26	1.29	1.12	0.89	1.54

Table 4
Average and associated standard deviation of microprobe analyses (wt.%) for serpentine phases from studied serpentinites.

Sample	ICHO2		RQ30		RQ23 serpentine				RQ16		RQ01		V6	
Grade	0		1		2				3		4		5	
Varieties	Ctl./Liz.		Ctl./Liz.		Atg. patches		Mixed mesh		Mixed/Atg.		Atg.		Atg.	
Concentration (wt.%)	n = 10	SD %	n = 10	SD %	n = 5	SD %	n = 4	SD %	n = 9	SD %	n = 8	SD %	n = 6	SD %
SiO_2	42.02	1.13	41.96	1.88	43.80	0.44	42.30	0.46	41.62	0.60	43.28	0.53	43.21	0.65
Al_2O_3	1.99	1.31	1.91	1.40	0.44	0.18	1.34	0.96	2.67	0.79	1.23	0.25	1.64	0.64
FeO	3.02	0.50	3.53	0.84	4.79	0.50	5.38	0.33	6.63	0.71	2.14	0.27	3.34	0.22
MnO	0.09	0.04	0.07	0.03	0.11	0.04	0.07	0.03	0.10	0.03	0.11	0.04	0.02	0.02
MgO	37.28	2.10	37.68	2.13	37.61	0.42	37.20	0.70	34.37	1.03	39.31	0.38	38.08	0.36
CaO	0.41	0.63	0.06	0.02	0.00	0.01	0.02	0.02	0.12	0.07	0.01	0.01	0.01	0.01
Na_2O	0.01	0.01	0.02	0.02	0.01	0.02	0.01	0.01	0.01	0.02	0.01	0.01	0.00	0.00
K_2O	0.02	0.01	0.01	0.01	0.02	0.02	0.01	0.01	0.01	0.01	0.02	0.01	0.01	0.01
TiO_2	0.06	0.05	0.03	0.02	0.00	0.01	0.02	0.02	0.03	0.03	0.01	0.01	0.01	0.02
NiO	0.11	0.07	0.15	0.08	0.23	0.02	0.22	0.02	0.13	0.01	0.09	0.01	0.06	0.06
Cr_2O_3	0.43	0.56	0.41	0.58	0.32	0.48	0.20	0.12	0.49	0.31	0.52	0.21	0.48	0.57
Total	85.44	0.52	85.84	1.57	87.33	0.27	86.78	0.58	86.18	1.24	86.74	0.48	86.86	0.84

Table 5
Representative trace element compositions (μg/g) of serpentine minerals, measured in situ (LA-HR-ICP-MS) (b.d.l.: below detection limit; n.d.: not detected).

Sample	ICH 02	ICH 02	ICH 02	RQ 30	RQ 30	RQ 30	RQ 23	RQ 23	RQ 16	RQ 16	RQ 01	RQ 01	V 6	V 6
Grade	0	0	0	1	1	1	2	2	3	3	4	4	5	5
# analysis	3	5	8	13	15	19	27	30	60	66	71	77	83	86
Spot size	102 μm	102 μm	102 μm	102 μm	102 μm	102 μm	102 μm	102 μm	102 μm	102 μm	102 μm	102 μm	102 μm	102 μm
Serpentine phase	Ctl.	Lz.	Lz.	Lz.	Lz.	Ctl.	Atg;	Lz.	Atg.	mixed	Atg.	Atg.	Atg.	Atg.
Primary mineral occurrence	Vein	Px bastite	Ol mesh	Px bastite	Ol mesh	Vein	Patch	Ol mesh	Vein	Ol mesh	Px bastite	Ol mesh	Px bastite	Ol mesh
Li	0.21	2.19	0.18	1.86	1.69	89.54	0.17	0.58	13.14	5.28	n.d.	n.d.	n.d.	n.d.
B	18.3	54.4	32.7	174.3	48.0	30.0	77.3	97.9	50.0	53.6	105.3	30.8	10.5	10.8
Ca	541.2	14,987	1428	639	318	1083	40	216	700	401	55	46	139	776
Sc	6.2	33.8	24.1	29.5	8.2	0.9	3.6	6.7	13.7	13.4	11.5	9.3	10.5	10.8
Ti	177.6	828.3	856.4	556.4	74.2	48.9	26.1	147.8	169.3	113.6	34.1	41.5	7.4	66.9
V	15.0	163.5	117.3	143.8	14.7	13.2	19.8	15.3	73.4	89.3	37.6	31.3	180.8	61.7
Cr	79.2	9053	6021	9835	665	321	433	776	2943	4087	4274	2249	18,385	1691
Co	48.8	14.1	52.1	51.4	64.1	25.8	79.2	51.3	42.4	52.4	52.7	72.5	85.6	58.1
Ni	661	833	946	2297	2165	182	2246	2434	1355	1309	995	1278	2132	565
Cu	1.1	n.d.	4.1	4.9	60.9	11.2	0.6	1.7	1.8	n.d.	4.9	8.8	0.7	0.7
Zn	24	36	30	30	19	67	28	23	34	36	39	36	42	32
Zn	20	29	25	27	17	56	25	20	31	32	32	31	35	29
As	0.07	b.d.l.	b.d.l.	0.15	b.d.l.	0.14	0.33	0.83	0.32	0.40	0.95	0.52	0.17	0.11
Rb	0.085	0.295	0.099	0.672	0.166	0.123	0.224	0.258	0.861	0.705	0.033	0.033	b.d.l.	n.d.
Sr	1.062	8.580	3.630	10.580	3.180	0.829	0.427	1.928	5.900	4.800	0.147	0.224	0.098	0.456
Y	1.260	4.170	2.321	2.963	0.840	0.102	0.048	0.455	3.630	2.781	0.243	0.345	0.022	0.145
Zr	0.175	1.537	0.872	0.765	0.271	0.030	0.122	1.139	1.548	1.047	n.d.	b.d.l.	0.109	0.636
Nb	n.d.	0.005	0.003	0.014	0.006	n.d.	0.003	0.013	0.007		0.003	n.d.	0.005	b.d.l.
Sb	n.d.	b.d.l.	n.d.	n.d.	0.01	n.d.	0.08	0.11	0.39	0.27	0.35	0.30	0.01	0.01
Cs	n.d.	b.d.l.	n.d.	0.88	0.21	0.13	0.53	1.10	4.42	3.47	n.d.	n.d.	n.d.	n.d.
Ba	b.d.l.	0.12	0.07	2.22	0.78	2.41	0.24	0.36	3.96	3.51	0.06	0.18	n.d.	n.d.
La	0.001	0.003	0.001	0.102	0.019	0.071	0.005	0.077	0.054	0.041	0.007	0.005	n.d.	0.002
Ce	0.006	0.022	0.017	0.393	0.090	0.196	0.019	0.176	0.261	0.210	0.016	0.005	n.d.	0.009
Pr	0.003	0.016	0.008	0.075	0.016	0.025	0.003	0.023	0.045	0.049	0.002	0.001	n.d.	n.d.
Nd	0.039	0.189	0.123	0.499	0.091	0.066	0.004	b.d.l.	0.385	0.347	0.011	0.006	n.d.	0.019
Sm	0.032	0.149	0.092	0.210	0.040	b.d.l.	b.d.l.	0.019	0.199	0.170	b.d.l.	b.d.l.	n.d.	0.008
Eu	0.013	0.047	0.032	0.073	0.010	0.013	n.d.	0.013	0.073	0.060	b.d.l.	n.d.	n.d.	n.d.
Gd	0.123	0.387	0.237	0.370	0.090	n.d.	b.d.l.	0.038	0.427	0.271	0.005	0.006	n.d.	0.010
Tb	0.020	0.081	0.048	0.074	0.016	n.d.	b.d.l.	0.009	0.076	0.070	0.003	0.005	n.d.	b.d.l.
Dy	0.180	0.724	0.386	0.563	0.143	n.d.	0.004	0.060	0.631	0.469	0.018	0.049	n.d.	0.016
Ho	0.048	0.166	0.095	0.136	0.032	b.d.l.	b.d.l.	0.014	0.150	0.104	0.008	0.015	0.001	0.001
Er	0.146	0.467	0.285	0.398	0.109	b.d.l.	b.d.l.	0.044	0.442	0.333	0.024	0.029	n.d.	0.003
Tm	0.019	0.073	0.036	0.058	0.020	n.d.	n.d.	0.012	0.065	0.051	0.004	0.007	n.d.	0.001
Yb	0.129	0.555	0.256	0.440	0.133	n.d.	0.005	0.084	0.393	0.338	0.029	0.042	n.d.	0.018
Lu	0.025	0.078	0.045	0.061	0.023	b.d.l.	0.001	0.014	0.068	0.044	0.006	0.008	b.d.l.	0.004
Hf	0.006	0.087	0.087	0.021	b.d.l.	n.d.	n.d.	0.017	0.107	0.048	n.d.	n.d.	n.d.	0.032
Ta	b.d.l.	n.d.	n.d.	0.0011	n.d.	n.d.	n.d.	n.d.	b.d.l.	n.d.	n.d.	n.d.	n.d.	b.d.l.
Pb	0.009	0.005	0.019	0.011	0.117	0.022	0.028	0.057	0.122	0.027	0.096	0.045	b.d.l.	0.292
Th	n.d.	n.d.	n.d.	n.d.	n.d.	n.d.	n.d.	0.000	n.d.	n.d.	n.d.	n.d.	n.d.	n.d.
U	n.d.	n.d.	n.d.	n.d.	b.d.l.	b.d.l.	0.001	0.001	n.d.	n.d.	b.d.l.	n.d.	n.d.	0.001

elements analyzed is between 280 cps/μg/g (Ni) and 23,000 cps/μg/g (Tb) based on measurements of the NIST 612 certified reference material. All the sensitivity values and detection limits are reported in Appendix 2. Oxide formation was monitored by measuring the ThO/Th ratio and was below 0.7%. Silicium-29 (^{29}Si) was used as an internal standard. The concentrations were calibrated against the NIST 612 rhyolitic glass using the values given in (Pearce et al., 1997). Data were subsequently reduced using the GLITTER software (Van Achterberg et al., 2001), using the linear fit to ratio method. Repeated analyses of references basalt BIR-1G allows us to assure measurement accuracy and reproducibility. Typically repeated analysis resulted in a 5 to 10% reproducibility (<1 sigma). Values of BIR-1G reference are reported in the Appendix 1 (preferred values from (Jochum et al., 2005; Jochum and Stoll, 2008)). Detection limits were below 0.08 μg/g, on average, for all elements except Ti (1 μg/g), Cr (0.2 μg/g) Ni (2.7 μg/g) Zn (0.5 μg/g). To eliminate values too close to the detection limit, we did a logical test ((values − 2 σ error) > detection limit). Representative trace element analyses are reported in Table 5; all results are reported in Appendix 2.

5. Results

5.1. Whole rock major and trace element compositions

5.1.1. Metasediments

Metasediments from the Schistes lustrés complex are very heterogeneous in terms of major elements (Fig. 3). They report important differences in L.O.I. (from 3.72 to 26.27 wt.%), SiO_2 (26.85–67.37 wt.%) and CaO (0.18–30.83 wt.%). We observe that the SiO_2 content decreases with metamorphic grade in the Schistes lustrés complex (from ~67.4 wt.% at Grade 1 to ~26.8 wt.% at Grade 4), whereas L.O.I. increases (from ~3.7 wt.% at Grade 1 to ~26.3 wt.% at Grade 4). The high L.O.I. variations reflect the important lithological heterogeneity, more specifically related to carbonate content (Fig. 3). The metasediments from Monviso ophiolite are more dehydrated and present lower carbonate content and a L.O.I. of approximately 10%.

Trace element compositions are relatively uniform in the samples from the Schistes lustrés complex, and the Monviso ophiolite (Fig. 4). All metasediments have a similar trace element pattern. All samples are light-REE enriched (LREE; ~100–200 times chondritic value) compared to the middle REE (MREE) and heavy REE (HREE; ~10 times chondritic value); the $(La/Yb)_N$ ratio varies from 8.7 to 17.7 and the $(La/Sm)_N$ ratio from 3.2 to 4.4 ($_N$ = normalized to C1-chondrite). One sample (RQ36) shows a slight concave-upward pattern from MREE to HREE (Fig. 4a). All samples are characterized by a well-marked negative Eu anomaly ($(Eu/Eu^*)_N$ from 0.58 to 0.85). Extended trace element patterns normalized to primitive mantle (PM, McDonough and Sun, 1995) (Fig. 4b) are characterized by slight enrichment in Pb and slight depletions in Ba and the high field strength elements (HFSE: Nb, Ta, Zr, Hf) relative to neighboring REE. Note that samples from the Monviso ophiolite (V11 and V15) are characterized by a stronger negative anomaly in Zr and Hf compared to other metasediments, as well as a negative anomaly in Sr that is also observable in samples RQ26, RQ28 and RQ36. Metasediments are enriched in fluid-mobile elements compared to primitive mantle. Sb, Cs, Pb and U present a strong enrichment relative to primitive mantle; Sb (0.16–1.26 μg/g; 30–230 × PM), Cs (5–10 μg/g; 100–500 × PM), Pb (10–45 μg/g; 60–300 × PM) and U (1–2 μg/g; 40–100 × PM). As and Li present a more moderate enrichment compared to primitive mantle: As (2.7–9.5 μg/g; 1.5–5 × PM) and Li (10–63 μg/g; 6–40 × PM), as well as Sr (20–500 μg/g; <25 × PM) (Table 3). The differences in Sr content are interpreted as related to the variation in carbonate content of our samples.

5.1.2. Serpentinites

Serpentinites have relatively uniform major element compositions (Table 3). Based on their SiO_2, MgO and Al_2O_3 concentrations, we assume that serpentinites derived from moderately refractory mantle protoliths with a depleted lherzolite composition ($1.14 < Mg/Si < 1.24$ and $0.02 < Al/Si < 0.07$). The MgO/SiO_2 and Al_2O_3/SiO_2 ratio of all studied serpentinites (Fig. 5a) are consistent with that of abyssal peridotites (e.g., Bodinier and Godard, 2007), and these observations confirm that these serpentinites have a common oceanic-lithosphere origin (Hattori and Guillot, 2007). The SiO_2 content increases slightly with metamorphic grade (from ~39.4 wt.% at Grade 0 to ~40.5 wt.% at Grade 5; Fig. 5b), whereas the L.O.I. tends to decrease (from ~13.2 wt.% at Grade 0 to ~11.6 wt.% at Grade 5; Fig. 5c). The low CaO contents (Fig 5d) probably reflect the combined effects of (i) a refractory protolith and (ii) serpentinization processes occurring in both oceanic and subduction environments, from low grade to HP-LT metamorphic conditions.

The chondrite-normalized (McDonough and Sun, 1995) REE concentration patterns (Fig. 6a) are variable; but overall slightly depleted. Samples from the Chenaillet ophiolite present two different patterns: ICH01 is characterized by depletion in LREE compared to HREE ($(La/Yb)_N = 0.08$), whereas ICH02 has a relatively flat pattern ($(La/Yb)_N = 1.21$) with a slightly positive Eu anomaly ($(Eu/Eu^*)_N = 1.27$) and a concave shape from the MREE to HREE. The extended trace element pattern normalized to PM (Fig. 6b) for sample ICH01 indicates a very slightly positive anomaly in Sr and Hf compared with the neighboring REE. For sample ICH02 there is a positive anomaly in Pb and, to a lesser extent, in Ba and U, whereas Nb and Ta are slightly depleted. Samples are depleted in incompatible trace elements compared to primitive mantle with the exception of sample ICH02, which is enriched in Sb (5 × PM).

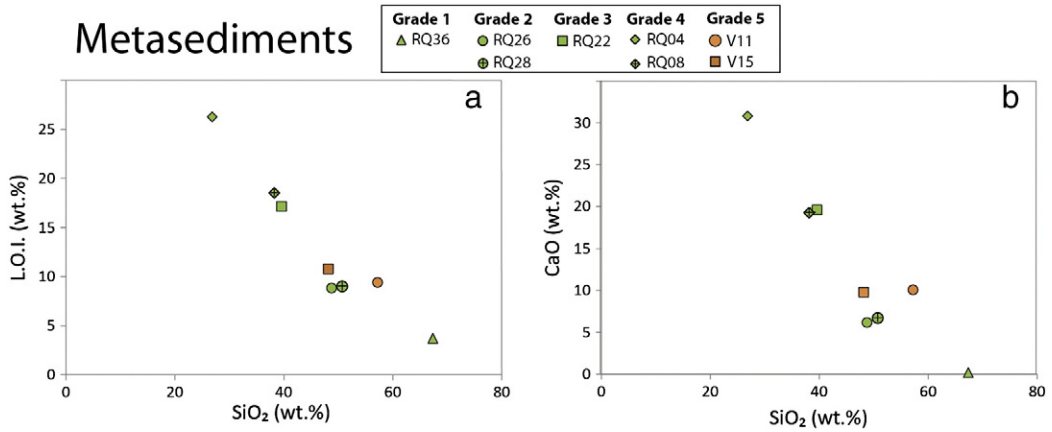

Fig. 3. (a) Whole rock (wt.%) L.O.I. and (b) CaO content in metasediments versus SiO_2. Grade 1 to Grade 4 samples come from the Schistes lustrés complex and Grade 5 samples from the Monviso ophiolite.

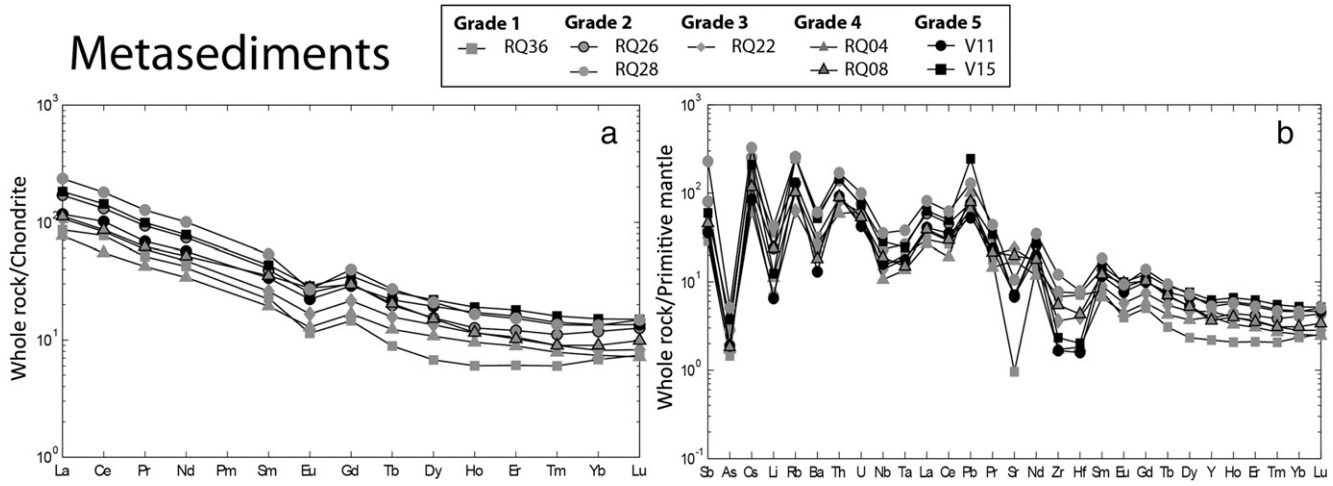

Fig. 4. (a) Chondrite-normalized (McDonough and Sun, 1995) REE concentrations and (b) primitive-mantle-normalized (McDonough and Sun, 1995) trace element concentrations of metasediments (results of whole rock analyses). Grade 1 to Grade 4 come from the Schistes lustrés complex and Grade 5 from the Monviso ophiolite.

Serpentinites from the Schistes lustrés complex can be divided in two groups. (1) RQ01 and RQ23 derived from a harzburgitic protolith and show a concave-upward pattern with a $(La/Yb)_N$ ratio of 0.57 and 1.01, respectively (Fig. 6a). (2) RQ16 and RQ30 are depleted in LREE compared to the HREE $(La/Yb)_N$ with ratios of 0.24 and 0.19, respectively. Based on these results we considered that group (2) samples have a higher clinopyroxene component and are characterized by a less refractory protolith. Only sample RQ23 has a positive Eu anomaly ($(Eu/Eu^*)_N = 1.73$). The extended PM-normalized trace element pattern (Fig. 6b) is characterized by a large positive Pb anomaly

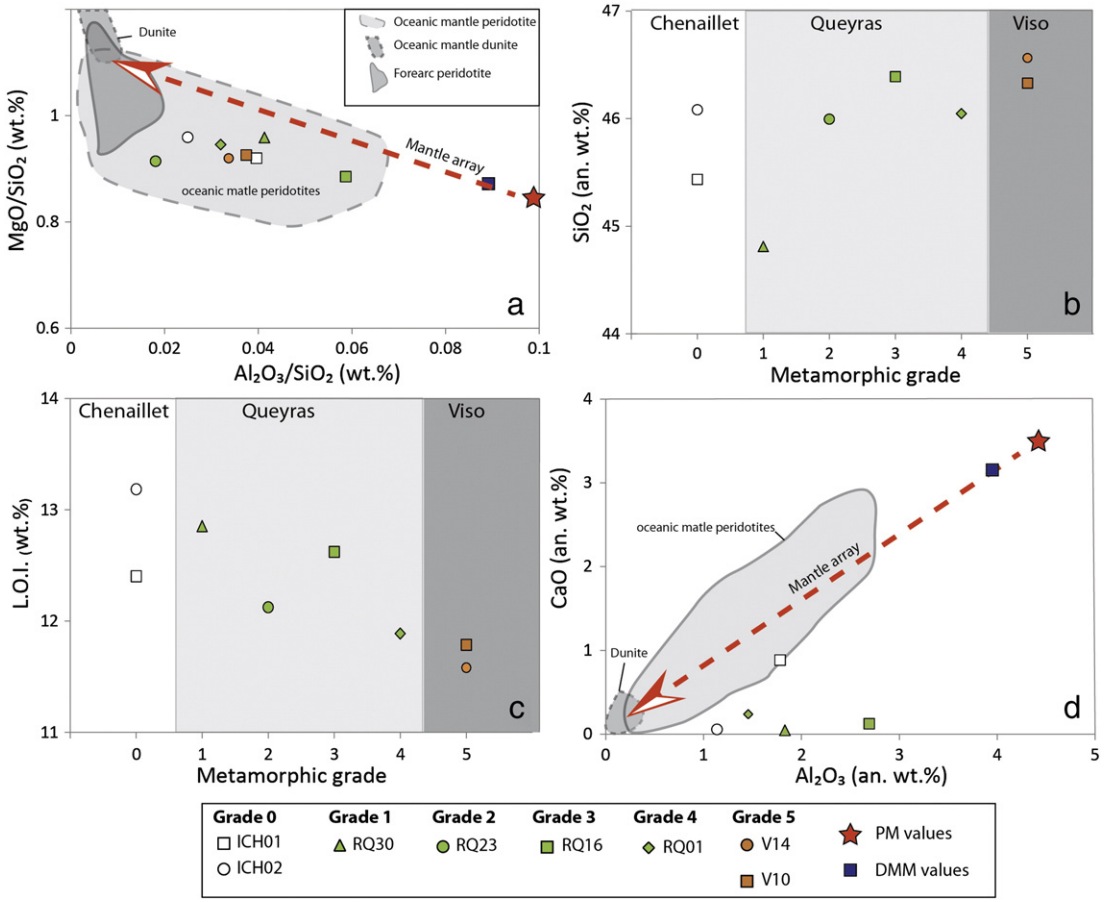

Fig. 5. (a) MgO/SiO_2 (wt.% ratio) versus Al_2O_3/SiO_2 (wt.% ratio) of bulk rock serpentinites, (b) Whole rock (anhydrous wt.%) SiO_2 and (c) L.O.I. content in serpentinites versus metamorphic grade, (d) CaO (anhydrous wt.%) versus Al_2O_3 (anhydrous wt.%). Data compilation for oceanic mantle peridotites and dunite and for marina forearc peridotites are from Bodinier and Godard (2007) and from Parkinson and Pearce (1998), respectively. Value from the primitive mantle and depleted MORB mantle are represented with red star and blue square (McDonough and Sun, 1995), mantle array from Jagoutz et al. (1979) is also reported.

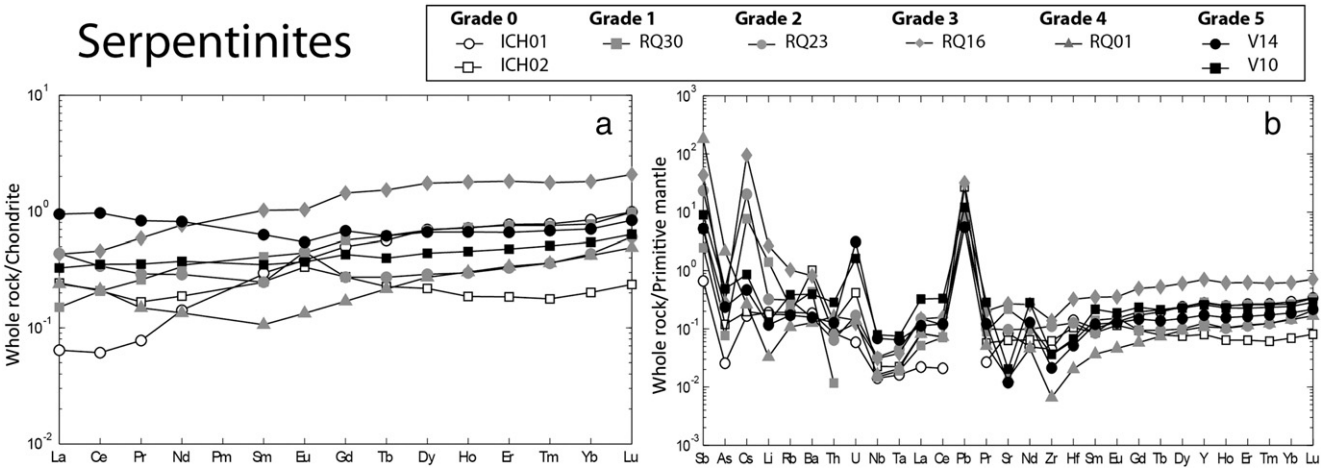

Fig. 6. (a) Chondrite-normalized (McDonough and Sun, 1995) REE concentrations and (b) primitive-mantle-normalized (McDonough and Sun, 1995) trace element concentrations of serpentinites (results from whole rock analyses). Grade 0 come from the Chenaillet, Grade 1 to Grade 4 come from the Schistes lustrés complex and Grade 5 from the Monviso ophiolite.

(except for RQ30), and all samples are systematically slightly depleted in Nb and Ta. RQ01 is depleted in Zr and Hf. All samples are enriched in Sb (2–200 × PM) and Cs (10–150 × PM) except RQ01.

The two samples from the Monviso ophiolite are quite similar, with nearly flat patterns (Fig. 6a), although V10 is slightly depleted in LREE compared to HREE ($(La/Yb)_N = 0.60$), and V14 has a slightly concave-upward pattern ($(La/Sm)_N = 1.51$ and $(Gd/Lu)_N = 0.81$). Both samples have positive U and Pb anomalies and negative anomalies in Sr, Zr, Hf, Nb and Ta on PM normalized extended trace element patterns. The two samples are depleted compared to the PM values, with the exception of Pb and U (respectively > 5 × PM values and 1.5–3 × PM values) and to a lesser extent Cs. Moreover, these two samples are systematically enriched in Sb (0.03–0.05 μg/g; 5–9 × PM values).

5.2. Composition of serpentine minerals

There are some noticeable differences in the major element composition between the serpentine species (Fig. 7). Table 4 presents the average and standard deviation of serpentine major element values. Lizardite displays a distinct wide range of compositions with respect to SiO_2 (38.7–44.2 wt.%), Al_2O_3 (0.5–4.7 wt.%), and MgO + FeO (36.7–43.8 wt.%), whereas antigorite has more uniform major element composition and a higher SiO_2 (42–43 wt.%) and MgO + FeO (41–44.3 wt.%) content. SiO_2 enrichment correlated with a depletion in Al_2O_3 is commonly describe during lizardite to antigorite transition (Dungan, 1979; Wunder et al., 2001; Fryer, 2002). This characteristic is particularly apparent in sample RQ23, where antigorite patches (Fig. 2c) are systematically richer in SiO_2 than the surrounding lizardite mesh.

Trace element compositions are extremely variable, with factor-of-ten differences in trace element concentrations on the thin section scale (Fig. 8). Nevertheless, and despite the extensive serpentinisation experienced by the studied samples, REE and some compatible elements allow the identification of three groups of serpentine REE patterns. This observation is consistent with previous studies that show that serpentine phases retain the geochemical signature of the primary minerals (Andréani et al., 2009; Deschamps et al., 2010). In this study, the nature of the primary mineral is deduced from pseudomorphic texture (bastite and mesh); hereafter we compare the REE-pattern of the different analyses with expected REE signatures based on literature values.

The serpentine species from Chenaillet (sample ICH02) display LREE-depleted chondrite-normalized REE-patterns in mesh and bastite (Fig. 8a), a characteristic that will be discussed in Section 6.1. The two bastite analyses reflect a clinopyroxene composition (e.g. Sun and Kerrich, 1995) with $(La/Yb)_N$ ratios of 0.0020 ± 0.0018 and a

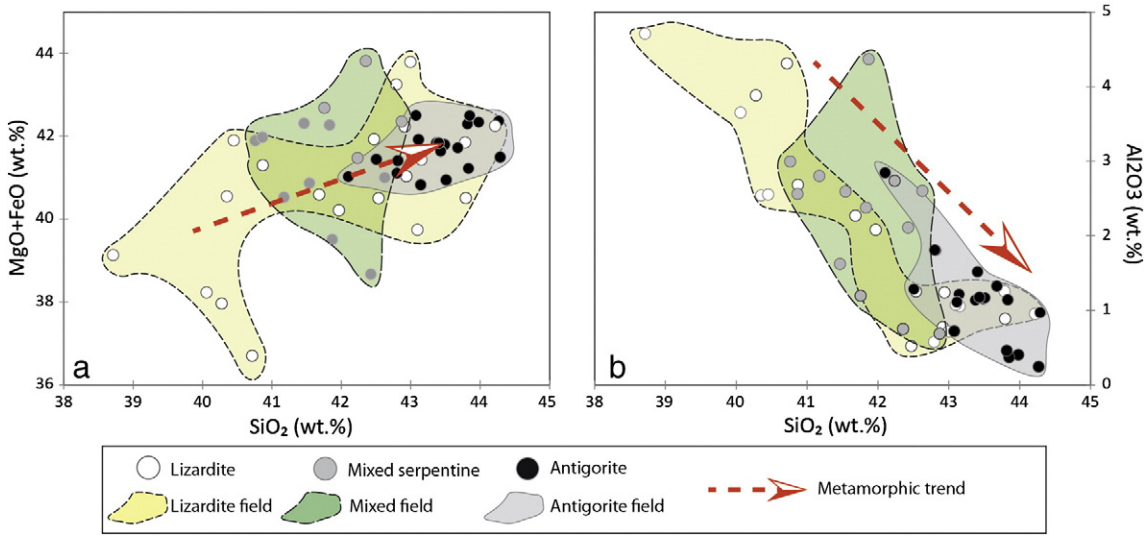

Fig. 7. (a) MgO + FeO and (b) Al_2O_3 contents (wt.%) of different serpentine minerals versus their SiO_2 content (wt.%).

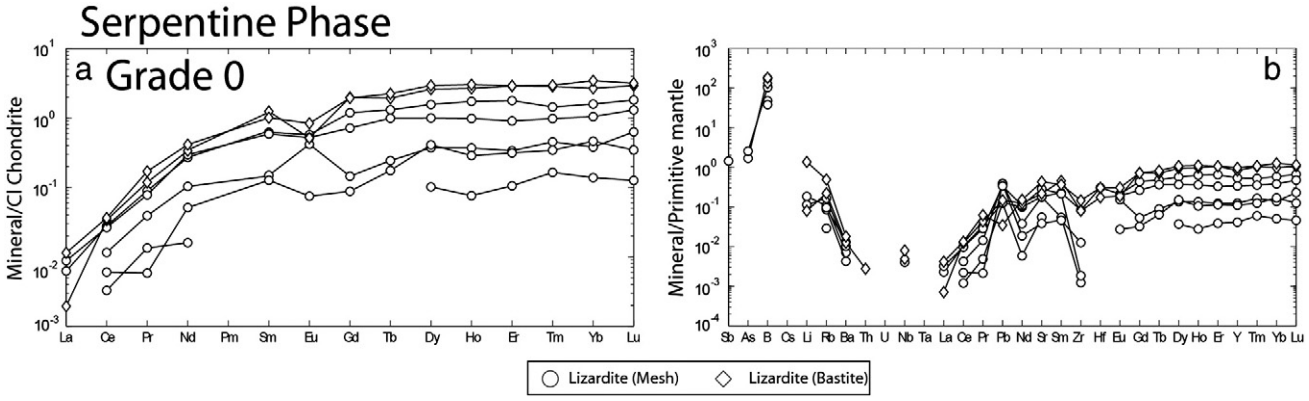

Fig. 8. Chondrite normalized REE (a) and primitive mantle normalized (McDonough and Sun, 1995) trace element contents (b) of serpentine of sample ICH02 (Chenaillet, Grade 0).

negative Eu anomaly ($(Eu/Eu^*)_N = 0.26 \pm 0.09$). Analyses made on mesh texture revealed REE-patterns with a strong depletion in LREE ($(La/Yb)_N = 0.004 \pm 0.002$) and Eu ($(Eu/Eu^*)_N = 0.70 \pm 0.45$), and indicates a lower enrichment in HREE than REE-patterns for bastite. All Chenaillet analyses display a strong enrichment in B compare to primitive mantle (6<B<55 μg/g; up to180 times PM) and a slight enrichment in As and Sb (only one sample where Sb has been detected) relative to primitive mantle, (0.06<As<0.12 μg/g; 1.5–2×PM and Sb = 0.008 μg/g; 1.5 times PM). Mesh serpentine contains more Pb than bastite serpentine (Fig. 8b). Serpentines from Chenaillet present a high heterogeneity in Li concentration. (0.1<Li<11 μg/g; 0.08–7×PM).

Serpentines from the Schistes lustrés complex present different patterns depending on their metamorphic grade and their initial mineralogy (Fig. 9). In sample RQ30, mesh serpentine has 2–4 times lower REE contents ($(La/Yb)_N = 0.10 \pm 0.04$) than bastite pseudomorphs ($(La/Yb)_N = 0.17 \pm 0.05$) presenting high HREE content. Mesh serpentines have a negative Eu anomaly $(Eu/Eu^*)_N = 0.41 \pm 0.02$. Bastites are systematically richer in fluid mobile elements (on average; As = 0.17 ± 0.04 μg/g, B = 200 ± 25 μg/g, Cs = 1.4 ± 0.4 μg/g and Li = 15 ± 12 μg/g) compared to mesh (on average As = 0.07 μg/g, B = 50 ± 19 μg/g, Cs = 0.17 ± 0.04 μg/g and Li = 0.8 ± 0.4 μg/g) with the exception of Pb. (Fig. 9b). Bastites display a negative anomaly in Pb, and mesh a positive anomaly. Enrichment in mobile elements compared to primitive mantle in mesh and bastite are respectively on average, ~1.4 and ~4 for As, ~150 and ~650 for B, ~8 and ~70 for Cs, ~0.6 and ~8 for Li. A small enrichment (~2×PM) in Rb is observed in bastites.

Sample RQ23 displays two types of REE-patterns after analysis of lizardite mesh and antigorite patches (Fig. 9c). $(La/Yb)_N$ in mesh and in the antigorite patch are approximately the same, (approximately 0.63), but antigorite patches are 10 times lower in concentration than lizardite mesh pseudomorphs. We also note a positive $(Eu/Eu^*)_N$ of 1.25 ± 0.4 in patches and 1.28 ± 0.55 in mesh. Like in REE, patchy antigorite is also depleted in other incompatible trace elements relative to the primitive mantle (Fig. 9d). PM-normalized spider diagrams display a positive anomaly in Pb, which is higher in patchy antigorite than in the lizardite mesh. Lizardite mesh is more enriched in Cs (35–75 times PM) than antigorite patches (11–44×PM). A strong positive anomaly in U is observed in one pattern (Analysis 43, see Appendix 2). The concentration of fluid-mobile elements is very homogeneous in mesh (Li = 0.7 ± 0.3 μg/g, B = 98 ± 25 μg/g, As = 0.8 ± 0.1 μg/g, Sb = 0.15 ± 0.04 μg/g). In patchy antigorite the concentrations of fluid-mobile elements are lower (0.2<Li<0.45 μg/g, B ~ 70 ± 9 μg/g, Sb = 0.1 ± 0.01 μg/g, As = 0.32 ± 0.09 μg/g).

The serpentine of RQ16 shows LREE-depleted chondrite normalized REE-patterns, regardless of its textural type/position. Mesh and bastite display approximately the same $(La/Yb)_N$ ratio = 0.086 ± 0.030 in mesh and 0.082 ± 0.007 in bastite. Patterns are generally enriched in HREE with $(Eu/Eu^*)_N = 0.43 \pm 0.04$ (Fig. 9e). Spider diagrams display a strong enrichment in fluid-mobile elements relative to primitive mantle (0.15<As<0.60 μg/g; 4–14 times PM, 0.15<Sb<1.20 μg/g; 27–225×PM and 0.5<Cs<8.0 μg/g; 100–400×PM, 2<Li<17 μg/g; 1.5–10.5×PM) (Fig. 9f).

Sample RQ01 is depleted in LREE and presents one type of pattern ($(La/Yb)_N = 0.16 \pm 0.10$ in mesh and 0.130 ± 0.025 in bastites) (Fig. 9g). Spider diagrams present a strong positive Pb anomaly (Fig. 9h). No Cs and Li were detected. B contents range from 30–65 μg/g in mesh and to 130 μg/g in bastite, this corresponds to enrichment between 80 and 400 in reference to the primitive mantle. Sb and As concentrations range between 0.2 and 1.0 μg/g corresponding to an enrichment between 3 and 20 for Sb and 20 and 65 for As referring to the primitive mantle.

Sample V6 from the Monviso ophiolite is characterized by one type of LREE-depleted pattern ($(La/Yb)_N = 0.070 \pm 0.035$) (Fig. 10a). Eu was not detected in all samples. PM-normalized spider diagrams are characterized by a positive Pb anomaly (Fig. 10b). We did not detect Li and Cs. The B concentration is approximately 12 μg/g, the As concentration ranges between 0.1 and 0.8 μg/g, and the Sb average concentration is 0.014 μg/g.

When veins are observed, REE concentrations are close to that of the whole rock. Veins systematically present a strong enrichment in Cs that increases with the metamorphic gradient. At the thin-section scale, a high concentration of Li and Cs is observed relative to mesh and bastite analysis (Fig. 11); these high concentrations are noticeable in chrysotile veins from RQ30 (Li = 60 ± 40 μg/g, Cs = 0.31 ± 0.16 μg/g), RQ16 (Li = 15.0 ± 1.5 μg/g, Cs = 5.0 ± 1.5 μg/g) and in the antigorite veins of RQ23 (45 μg/g for Li and 1.7 μg/g for Cs).

A noticeable decrease in Sr content is observed at the lizardite/antigorite transition and in the most strongly metamorphosed samples (Fig. 11). The different serpentine varieties are systematically depleted in Th, Nb, Ta and Zr, except for RQ23 in which no Zr anomaly is observed. The consistency between the trace element characteristics of the whole rocks and the corresponding individual serpentine minerals suggests that the latter host most of the trace elements, and that potential micro-phases play only a minor role. Concerning Monviso samples, the differences between serpentine in situ trace element concentrations and bulk rock abundances (especially for Li and Cs) could be explained by the presence of secondary metamorphic phases such as chlorite or sulfides which trap certain trace elements more efficiently than antigorite.

6. Discussion

6.1. Chenaillet (Grade 0): from ridge to obduction

In all samples, especially those coming from the Chenaillet, pseudomorphic texture (mesh) is systematically observed. This texture is related to a static hydration of peridotite by seawater, reflecting

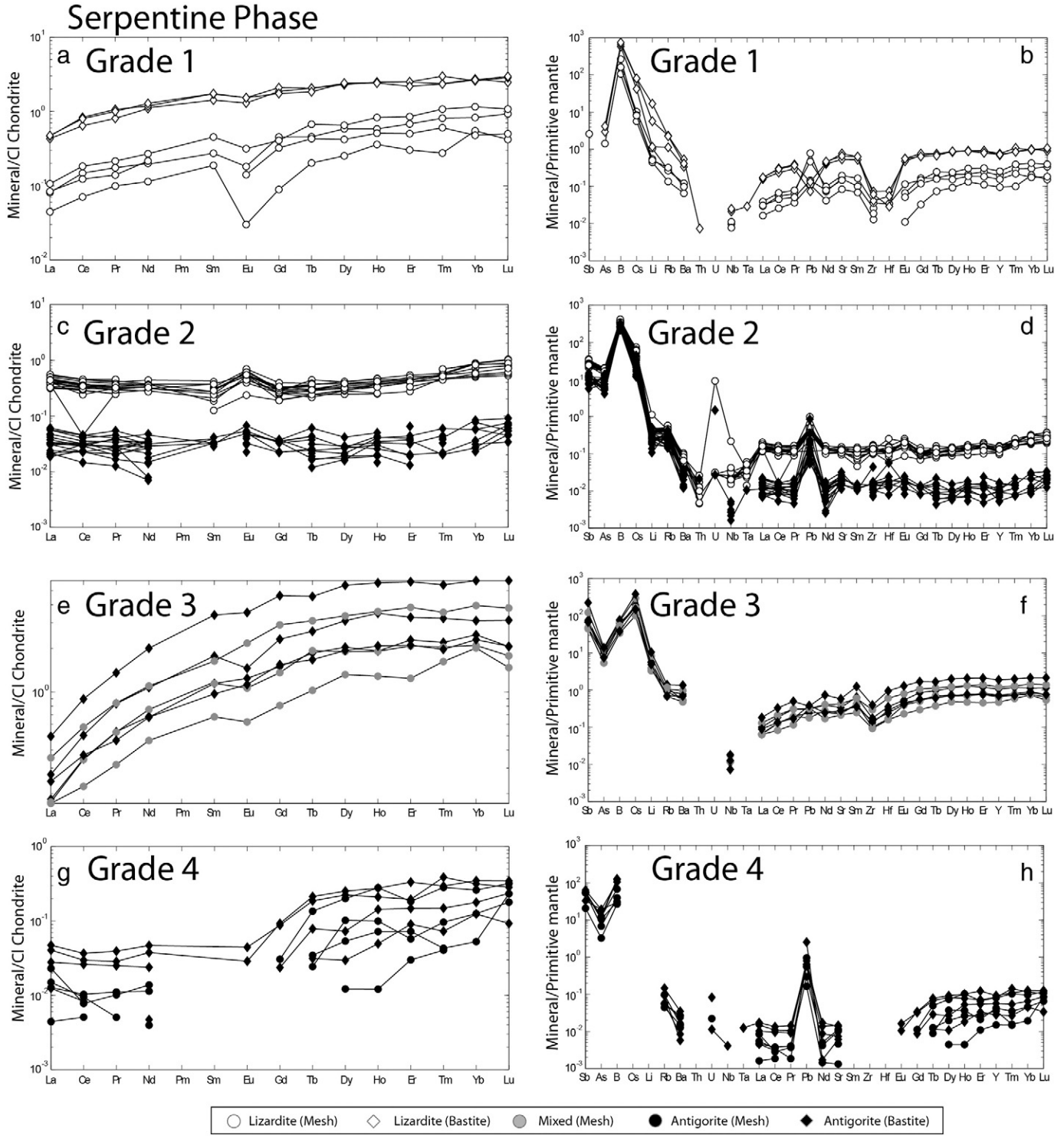

Fig. 9. Chondrite normalized REE (a, c, e, g) and primitive mantle normalized (McDonough and Sun, 1995) trace element contents (b, d, f, h) of serpentine of samples RQ30 (a, b; Rocher Blanc, Grade 1), RQ23 (c, d; Rocca Bianca, Grade 2), EQ16 (e, f; Eychassier, Grade 3) and RQ01 (g, h; Refuge du Viso, Grade 4).

serpentinization processes occurring in oceanic ridge environment (Moody, 1976; Fryer, 2002; Mével, 2003) and/or during static serpentinization during obduction processes. In the Chenaillet ophiolite (Grade 0), mesh texture is dominated by a low grade lizardite and chrysotile assemblage. The major element compositions of the Chenaillet samples are characteristic of a depleted lherzolite protolith ($0.02 < Al/Si$ weight ratio < 0.06) (Rehkämper and Hofmann, 1997), typical of slow-spreading ridges (Dick et al., 2003). This composition has already been shown for alpine peridotites (Hattori and Guillot, 2007). However, REE patterns of the two samples from the Chenaillet are different and probably reflect chemical heterogeneities in the protoliths. The trace element compositions in the Chenaillet serpentinites display a limited enrichment in fluid-mobile elements relative to PM with the exception of B and Pb (Figs. 6 and 11), which is in agreement with serpentinization occurring in an abyssal environment dominated by seawater interactions (Paulick et al., 2006; Vils et al.,

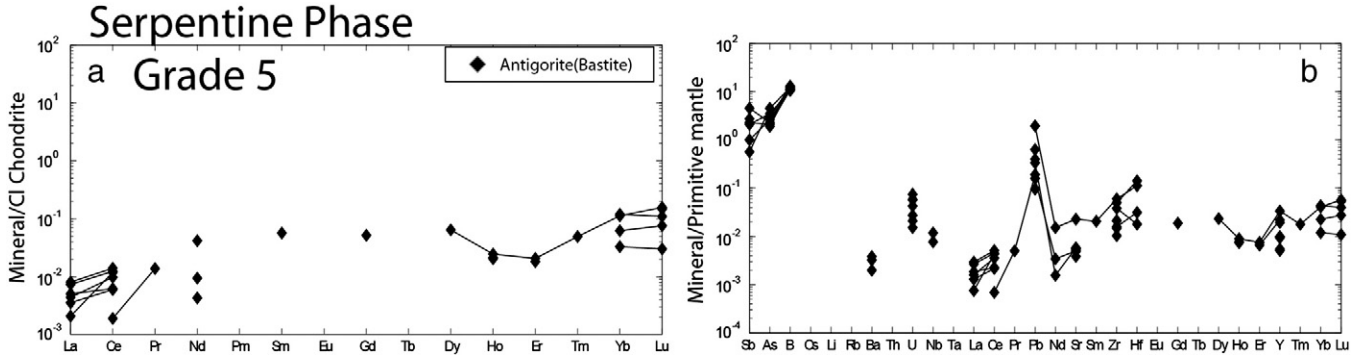

Fig. 10. Chondrite-normalized REE (a) and primitive-mantle-normalized (McDonough and Sun, 1995) trace element concentrations in antigorite of V6 (Grade 5; Monviso ophiolite).

2008, 2009; Kodolányi et al., 2012). This restricted enrichment in fluid-mobile elements is superimposed on a strongly depleted trace element composition of the initial protolith.

Chenaillet serpentines display a strongly depleted LREE pattern and high variability in HREE (Fig. 8a). Such REE-patterns are reminiscent of those found in serpentine that formed after clinopyroxene in forearc serpentine (Deschamps et al., 2010). Here, we find that the initial mineralogy deduced from textural characterization (mesh texture after olivine) is not systematically associated with a specific REE signature after serpentinization. The circulation of fluids through the activation of veins could be an important factor in homogenizing serpentine REE-patterns and redistributing some trace elements. Veins are more enriched in fluid-mobile elements than pseudomorphic serpentine (Fig. 11).

6.2. Monviso serpentinites (Grade 5): fluid-mobile element transfer in subduction systems

The Monviso ophiolite is an exhumed unit from the serpentinite subduction channel. The associated serpentines are depleted in fluid-mobile elements and present concentrations close to that of serpentines from the Chenaillet ophiolite. Serpentines are systematically less enriched in fluid-mobile elements compared to serpentines from the Schistes lustrés complex, (10×PM for B, 1–5×PM for As and Sb) and are completely devoid of Li and Cs (Fig. 13).

Partial antigorite dehydration is observable under eclogitic conditions (temperature > 480 °C) as shown by the presence of metamorphic olivines and chlorite (Schwartz et al., 2013) that could contain high trace element concentrations. The absence of Si-rich phases could be explained by Al- and Si-rich fluid being released during the high pressure antigorite dehydration (Scambelluri et al., 2001). A part of the decrease in fluid-mobile elements could be explained by such a fluid release. Peacock, 1990, 1993 showed that a "slab" subducted under eclogitic facies conditions experiences strong dehydration at the blueschist-eclogite transition. Also Spandler et al. (2011) show that secondary eclogitic veins in the Monviso ophiolite are enriched in fluid-mobile elements, and they proposed that serpentinite-derived fluids are capable of infiltrating more than tens of meters into mafic eclogite and can impart characteristic subduction-type geochemical signatures in fluid-mobile elements, such as B, As and Sb. We propose that the main factor that must be considered is the scarcity of metasediments, which represent less than 10% of the massif (Schwartz et al., 2001). Previous studies realized on Himalayan serpentinites associated with eclogitized rocks from Tso Morari (Hattori and Guillot, 2003;

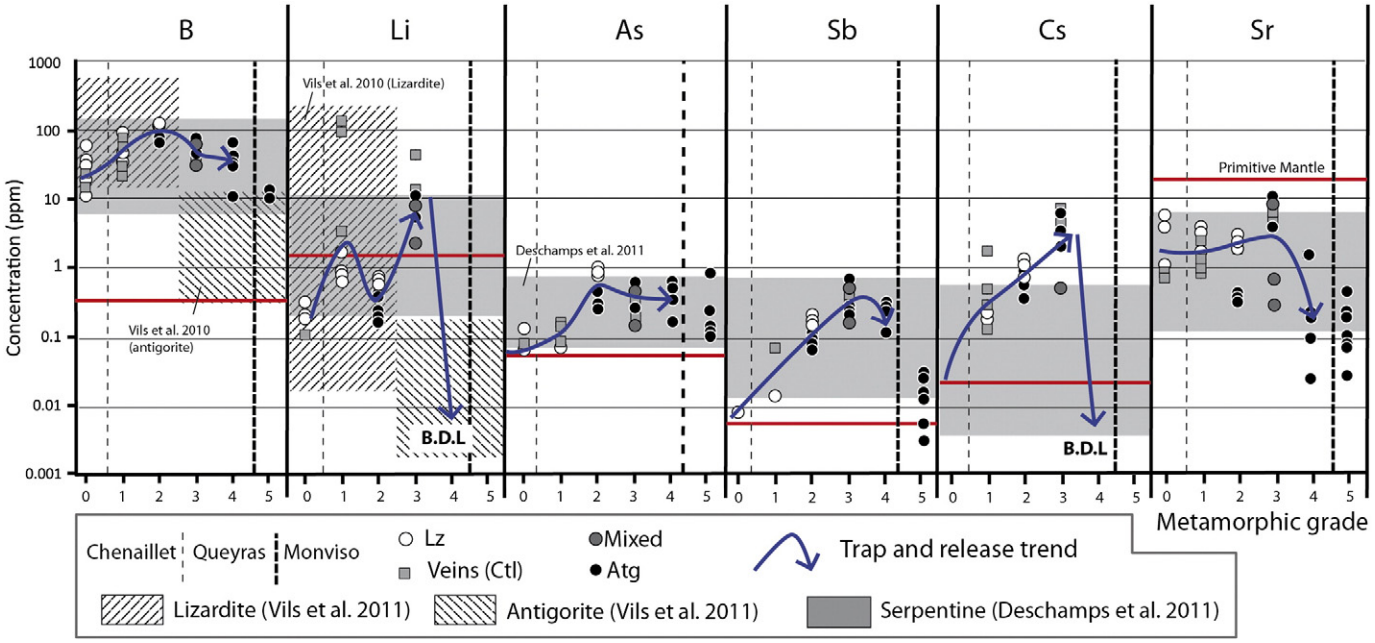

Fig. 11. Plots of concentrations of selected fluid-mobile elements (B, Li, As, Sb, Pb, Cs and Sr) in serpentines from the Schistes-lustrés unit along a metamorphic gradient. Values of primitive mantle after McDonough and Sun (1995) are reported (red line). Gray horizontal fields represents data from Deschamps et al. (2011), fields with slanting lines represent data obtained on lizardite and antigorite from Vils et al. (2011). (For interpretation of the references to color in this figure legend, the reader is referred to the web version of this article.)

Deschamps et al., 2010) indicate a high enrichment in Li and Cs (up to 10×PM) and extremely high As and Sb contents (up to 1000×PM). Based on the trace element distributions and Pb isotope data, Deschamps et al. (2010) concluded that most of the excess fluid mobile elements in these serpentinites are brought into the system from surrounding sediments. Therefore metamorphism and dehydration are not the only explanations for low fluid mobile element concentrations. In the case of Monviso serpentinites, the lack of sediments in this area suggests that the serpentinites did not exchange with surrounding metasediments within the subduction channel and did not acquire a strong enrichment in fluid-mobile elements compared to oceanic serpentinites.

Serpentinites from Monviso ophiolite could be considered as a potential source of fluids at depth. These fluids may migrate through the mantle wedge above the subducting plate and bring a particular signature to forearc rocks and volcanic arc magmas. Indeed, serpentinized peridotites from Mariana forearc displayed fluid-mobile element enrichment consistent with the release of fluids, in particular B, As, Cs and Li (Savov et al., 2007), from the subducting plate under HP/LT conditions.

6.3. Schistes lustrés serpentinites (Grade 1 to 4): A trap-and-release system

The transition from low-grade serpentine species (chrysotile, lizardite) to antigorite is controlled by dissolution recrystallization processes (Auzende et al., 2006) occurring in mesh texture at primary olivine grain boundaries where magnetite is present. The result is an increase in Si content coupled with a decrease in Al. This process is accompanied by a homogenization of the serpentinite system from high chemical variability in lizardite to low chemical variability in antigorite, until the high Si/Al ratio end member is reached (Fig. 7). Our finding is consistent with the reaction 16 Lz/Ctl + 2 SiO_2aq = Atg + H_2O, marked by silica enrichment (1–2%), and with dehydration (~2%) (Dungan, 1979; Evans, 2004) inducing an homogenization of the serpentinite system. Iron oxide crystallization (e.g. magnetite, hematite) and changes of iron oxidation state during the serpentinization processes (Evans, 2010; Evans et al., 2012) could play a major role and must be considered for element remobilization during metasomatism and metamorphism under increasing P–T conditions.

In this study, we show that serpentinites experienced a strong enrichment in fluid-mobile elements during subduction processes in the Schistes lustrés complex (Grades 1 to 4). Serpentinites from the Schistes lustrés complex display a high enrichment in B (30–800× PM), Cs and Sb (40–500×PM) and a moderate enrichment in Li and As (5–15×PM) up to Grade 3. The results are consistent with those from recent studies (Deschamps et al., 2011, 2012; Kodolányi and Pettke, 2011; Vils et al., 2011), highlighting that subducted serpentinites are similar to mid-ocean ridge serpentinites with respect to overall trace element depletion and are marked by As, B, Sb, Pb and Li enrichment (Fig. 12). No strong positive anomalies in U or Sr were observed, similar to what was observed in the subduction-related serpentinites from the Himalaya (Deschamps et al., 2010) or Greater Caribbean (Deschamps et al., 2011).

Fluid-mobile element enrichment observed in the Schistes lustrés serpentinites ranges between 100 and 1000 times that of PM for B, As, Sb and Cs. Enrichment follows the increasing metamorphic grade from west to east (Fig. 12). This strong enrichment is clearly related to subduction and not to oceanic hydration. Enrichment remains very low through the lizardite/antigorite transition (Grade 2 to Grade 3), as fluid-mobile element concentrations achieve their maxima in rocks with lizardite and antigorite (Fig. 11). This is comparable with previous studies (e.g. Vils et al., 2009; Kodolányi and Pettke, 2011) that have suggested that fluid-mobile element contents and REE spectra may be influenced not only by primary mineralogy but also by the lizardite/chrysotile-to-antigorite transition.

Our results indicate that the increase of metamorphic conditions coupled to the lizardite to antigorite transition (Grade 4) implies a stop or a slight depletion of B, Sb and As. Fluid-mobile elements appear to not be incorporated above a temperature of 390–400 °C where antigorite is the only serpentine phase. A threshold is generally observed for fluid-mobile elements, 100 μg/g for B and 0.3 and 1.0 μg/g, respectively, for As and Sb (Fig. 11). Moreover, in this study Li and Cs appear to be more mobile than the other elements as they are completely released out of the serpentinite system above 360 °C (Grade 4, Fig. 11, below detection limit). Deschamps et al. (2010) indicate that As and Sb are released early in forearc mantle wedge serpentinites while Li, Cs and Pb are released deeper, which is the opposite of our observations. The loss of Sr could reflect the onset of serpentinite dehydration leading to the release of initial Sr hosted by primary serpentinites. This dehydration may lead to Sr-rich fluid release in open systems instead progressively increasing Sr contents in serpentinites from metamorphic units.

However, the lizardite-to-antigorite transition appears to be not the only factor influencing the release of fluid-mobile elements. Our results indicate that while As and B concentrations stop increasing after the first occurrence of antigorite, the concentrations of the other fluid-mobile elements continue to increase (Fig. 11). These contrasting results could be explained by the difference in the emplacement of the serpentinites between the two studies. Our samples are imbricated within metasediments while those studied by Vils et al. were taken from an ophiolite sequence, where sediments are rare or located far from the sample sites.

The most important parameter influencing the chemistry of serpentinites appears to be the great volume of surrounding metasediments. Fluid-mobile element enrichment observed in serpentinites from the Schistes lustrés complex is consistent with hydration in a sediment-dominated environment and a high fluid/rock ratio (Deschamps et al., 2011). The composition of fluids might be a function

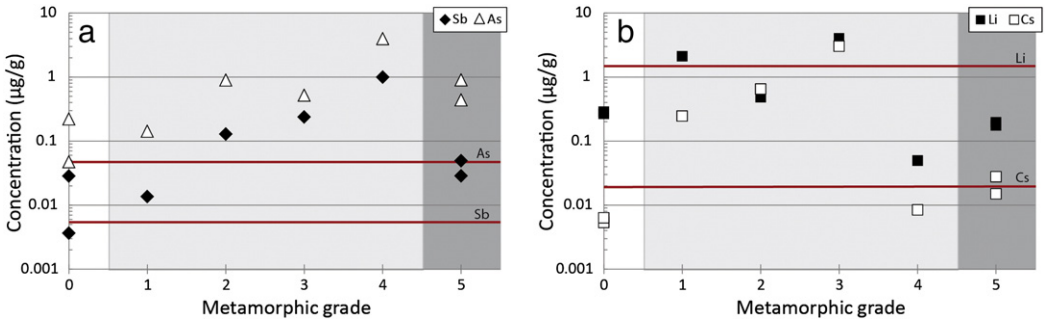

Fig. 12. Whole rock trace element content in serpentinites (μg/g). (a) As and Sb contents, (b) Li and Cs contents. Evolution is represented along the metamorphic gradient. White area for samples from Chenaillet, gray area for samples from Schistes lustrés complex and dark gray area for samples from Monviso. Values of primitive mantle after McDonough and Sun (1995) are reported (red line) with corresponding element. (For interpretation of the references to color in this figure legend, the reader is referred to the web version of this article.)

of the age and the type of sediments as suggested by You et al. (1996). The strong enrichment observed in the Schistes lustrés complex is thus explained by the high metasediment/serpentinite volume ratio (approximately 9–10 based on the mapping study) and the increasing metamorphic gradient (Figs. 11 and 12). The chemical results obtained on metasediments are difficult to interpret due to the high initial heterogeneity of the protoliths. The Li/Ce and Cs/Ce ratios in sediments decrease with the metamorphic grade, but it is difficult to determine whether this trend is related to the release of fluid-mobile elements or due to the large initial chemical heterogeneity of the sediments. Bebout et al. (1999) highlight a loss of volatile elements in the metasediments of the Catalina schists (West Coast USA) under increasing P–T conditions. In our study, due to the high metasediment/serpentinite volume ratio the enrichment observed in serpentinites is not balanced by a noticeable depletion trend in metasediments. We propose that, between 300 and 400 °C, fluid-mobile elements are released from the Schistes lustrés sediments and are preferentially incorporated in lizardite during its recrystallization. The plateau observed for some elements (B, As, Sb) is not due to a lack of availability of these elements, as the sediments constitute a nearly endless supply (Table 3), but could be a threshold effect due to the structural properties of serpentine as antigorite progressively replaces lizardite.

In our study we observe two opposite effects acting together. One is the existence of a threshold and the release of fluid-mobile elements due to the lizardite to antigorite transition as metamorphic grade increases. The other is the trapping of volatiles and mobile elements derived from metasediment dehydration (You et al., 1996; You and Gieskes, 2001). A temperature range between 300 °C and 390 °C (Grades 1–3) is required for trace-element exchange within an accretionary wedge zone, as some elements (As, Sb, and B) are trapped within serpentine. Strontium, for example, is released at a temperature > 360 °C (Grade 4). Other elements (Li and Cs) have intermediate behavior, with enrichment from 300 to 360 °C (Grades 1–2); these elements are released at higher temperatures (Fig. 13).

7. Conclusions

Trace element compositions of exhumed serpentinites along a paleo-subduction metamorphic gradient give an understanding of the behavior of fluid-mobile elements during subduction processes. Incorporation, or release of fluid-mobile elements in the serpentine species is dependent on the proximity of metasediments and/or metamorphic conditions. In an oceanic environment (Chenaillet ophiolite), we observe an initial serpentinization associated with the replacement of primary peridotites by the lizardite/chrysotile assemblage. This is the result of the interaction with seawater and slight enrichment of trace elements, especially in Sr and B, between 200 and 300 °C. In the accretionary wedge (Schistes lustrés complex), a second

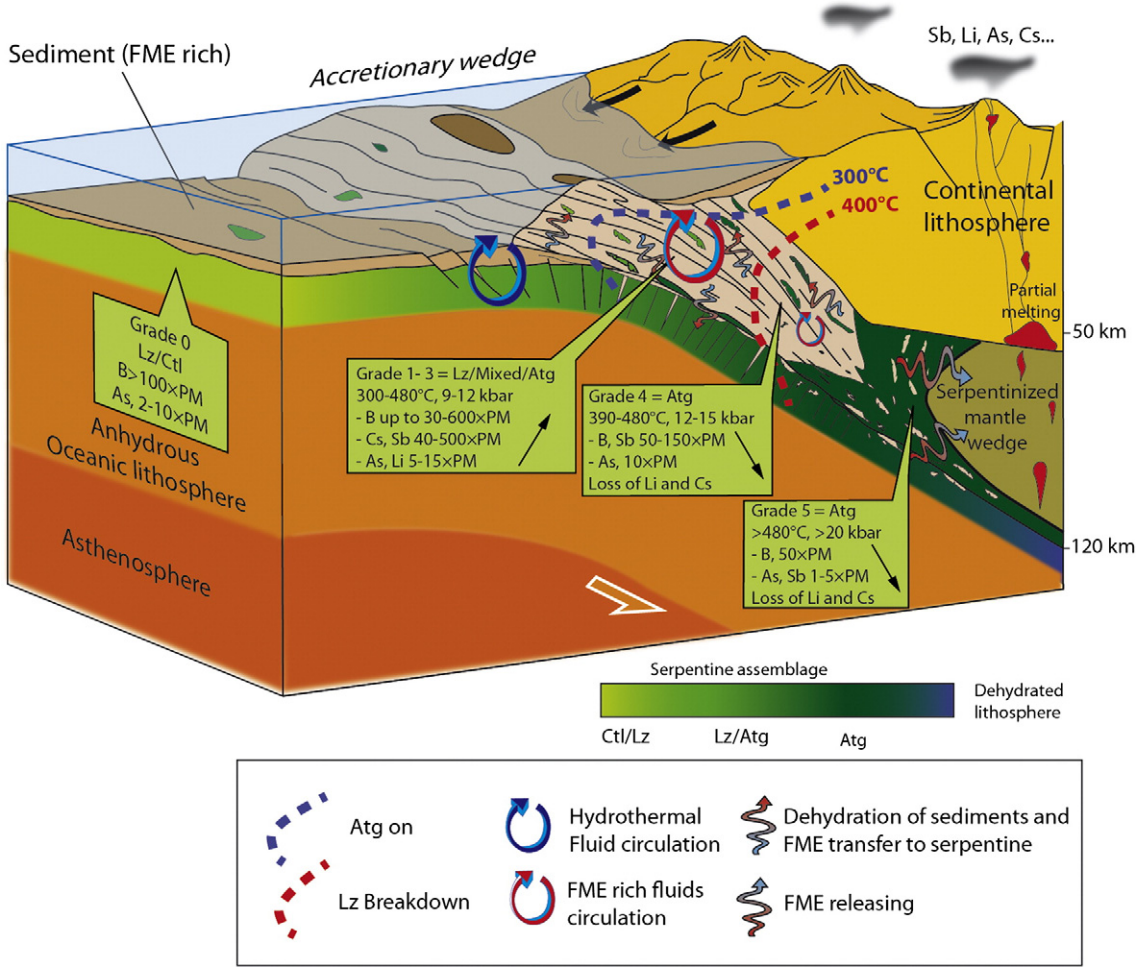

Fig. 13. Schematic illustration of serpentinization processes occurring in an accretionary context. Samples from Grade 0 corresponds to serpentinized peridotites close to a slow-spreading ridge (Deschamps et al., 2011). Second serpentinization occurs at the core of an accretionary wedge during their structuration (Grades 1 to 4). In this context, a high sediment component contributes to fluid-mobile elements enrichment of serpentinites along the metamorphic gradient imposed by the transport at depth of serpentinized mantle. Second serpentinization is characterized by the transition from lizardite/chrysotile assemblage to antigorite. Serpentinites from slab, carried lower content of fluid-mobile elements to depth and may be incorporated within the subduction chanel (Grade 5). Fluid-mobile elements can efficiently be transferred to the mantle wedge and contribute to arc magma volcanoes signature (Hattori and Guillot, 2003).

serpentinization stage occurred at a shallow subduction depth and corresponds to the gradual formation of antigorite at the expense of the lizardite/chrysotile assemblage. The lizardite/chrysotile assemblage disappears at ~390 °C. This secondary serpentinization process is associated with significant geochemical exchange. Sediments are a source of fluid-mobile-elements for the enrichment of surrounding serpentinites via silica-rich fluids circulation. Fluid-mobile elements are released from metasediments and incorporated into serpentinites. In this general trend, the specific behavior of each fluid-mobile element is unique and temperature dependent. The element Sr is enriched mainly in the oceanic environment, and then remains immobile to 360 °C, before being mobilized. The elements B, Li, and Cs are enriched in the subduction environment up to ~360 °C, and then they are released, while As and Sb are enriched up to 390 °C, then released. In the serpentinized subduction channel (Monviso ophiolite), no additional fluid-mobile element enrichment is observed. The low abundance of fluid-mobile elements is related either to the absence of metasediments and/or to the onset of serpentinite dehydration, allowing the fluid-mobile elements to be released. We emphasize that the lithology within the subduction system is largely responsible for the observed geochemical differences. Serpentinites, from oceanic ridge to subduction channel, act as a trap-and-release system and can transfer fluid-mobile elements into the sub-arc. The release of fluid-mobile elements due to antigorite breakdown can allow the enrichment of the mantle wedge and input a specific sedimentary signature to arc magmas.

Supplementary data to this article can be found online at http://dx.doi.org/10.1016/j.chemgeo.2013.02.008.

Acknowledgments

This study was supported by the CNRS, the ANR-08-BLAN-0303-01 ERD-Alps and the Labex OSUG2020. We thank Keiko Hattori for fruitful discussions. We thank the reviewers (János Kodolányi and Flurin Vils) and the editor (Laurie Reisberg) for fruitful comments that help us to improve the quality of this paper.

References

Agard, P., Jolivet, L., Goffé, B., 2001. Tectonometamorphic evolution of the Schistes Lustres Complex; implications for the exhumation of HP and UHP rocks in the Western Alps. Bulletin de la Société Géologique de France 172, 617–636.

Agard, P., Monié, P., Jolivet, L., Goffé, B., 2002. Exhumation of the Schistes Lustrés complex: in situ laser probe $^{40}Ar/^{39}Ar$ constraints and implications for the Western Alps. Journal of Metamorphic Geology 20, 599–618.

Andréani, M., Mével, C., Boullier, A.M., Escartin, J., 2007. Dynamic control on serpentine crystallization in veins: constraints on hydration processes in oceanic peridotites. Geochemistry, Geophysics, Geosystems 8, Q02012. http://dx.doi.org/10.1029/2006GC001373.

Andréani, M., Godard, M., Mével, C., 2009. LA-(HR-)ICPMS study of serpentinites from ODP Site 920 (23°N MAR): insights on transfers and trace element distribution during serpentinization. Geophysical Research Abstracts 11, EGU2009–EGU13248.

Angiboust, S., Agard, P., Raimbourg, H., Yamato, P., Huet, B., 2011. Subduction interface processes recorded by eclogite-facies shear zones (Monviso, W. Alps). Lithos 127, 222–238.

Auzende, A.L., Guillot, S., Devouard, B., Baronnet, A., 2006. Serpentinites in an Alpine convergent setting: effects of metamorphic grade and deformation on microstructures. European Journal of Mineralogy 18, 21–33.

Bebout, G.E., Ryan, J.G., Leeman, W.P., Bebout, A.E., 1999. Fractionation of trace elements by subduction-zone metamorphism — effect of convergent-margin thermal evolution. Earth and Planetary Science Letters 171, 63–81.

Bodinier, J.L., Godard, M., 2007. Orogenic, ophiolitic, and abyssal peridotites. Treatise on Geochemistry. Pergamon, Oxford, pp. 1–73.

Bonatti, E., Lawrence, J.R., Morandi, N., 1984. Serpentinization of oceanic peridotites: temperature dependence of mineralogy and boron content. Earth and Planetary Science Letters 70, 88–94.

Carignan, J., Hild, P., Mevelle, G., Morel, J., Yeghicheyan, D., 2001. Routine analyses of trace elements in geological samples using flow injection and low pressure on-line liquid chromatography coupled to ICP-MS: a study of geochemical reference materials BR, DR-N, UB-N, AN-G and GH. Geostandards Newsletter 25, 187–198.

Deschamps, F., Guillot, S., Godard, M., Chauvel, C., Andréani, M., Hattori, K., 2010. In situ characterization of serpentinites from forearc mantle wedges: timing of serpentinization and behavior of fluid-mobile elements in subduction zones. Chemical Geology 69, 262–277.

Deschamps, F., Guillot, S., Godard, M., Andréani, M., Hattori, K., 2011. Serpentines act as sponges for fluid-mobile-elements in abyssal and subduction zone environments. Terra Nova 23, 171–178.

Deschamps, F., Godard, M., Guillot, S., Chauvel, C., Andréani, M., Hattori, K., Wunder, B., France, L., 2012. Behavior of fluid-mobile elements in serpentines from abyssal to subduction environments: examples from Cuba and Dominican Republic. Chemical Geology 312, 93–117.

Dick, H.J.B., Lin, J., Schouten, H., 2003. An ultraslow-spreading class of ocean ridge. Nature 426, 405–412.

Dungan, M., 1979. A microprobe study of antigorite and some serpentine pseudomorphs. The Canadian Mineralogist 17, 771–784.

Evans, B.W., 2004. The serpentinite multisystem revisited: chrysotile is metastable. International Geology Review 46, 479–506.

Evans, B.W., 2010. Lizardite versus antigorite serpentinite: magnetite, hydrogen, and life(?). Geology 38, 879–882.

Evans, B.W., Dyar, M.D., Kuehner, S.M., 2012. Implications of ferrous and ferric iron in antigorite. American Mineralogist 97, 184–196.

Fryer, P., 2002. Recent studies of serpentinite occurrences in the oceans: mantle–ocean interactions in the plate tectonic cycle. Chemie der Erde-Geochemistry 62, 257–302.

Godard, M., Jousselin, D., Bodinier, J.-L., 2000. Relationships between geochemistry and structure beneath a palaeo-spreading centre: a study of the mantle section in the Oman ophiolite. Earth and Planetary Science Letters 180 (1–2), 133–148.

Goffé, B., Schwartz, S., Lardeaux, J.M., Bousquet, R., 2004. Explanatory notes to the map: metamorphic structure of the Alps Western and Ligurian Alps. Mitteilungen der Österereichischen Mineralogischen Gesellschaft 149, 125–144.

Gunther, D., Heinrich, C., 1999. Enhanced sensitivity in laser ablation-ICP mass spectrometry using helium–argon mixtures as aerosol carrier. Journal of Analytical Atomic Spectrometry 14, 1363–1368.

Handy, M.R., Schmid, M.S., Bousquet, R., Kissling, E., Bernoulli, D., 2010. Reconciling plate-tectonic reconstructions of Alpine Tethys with the geological–geophysical record of spreading and subduction in the Alps. Earth-Science Reviews 102, 121–158.

Hattori, K., Guillot, S., 2003. Volcanic fronts form as a consequence of serpentinite dehydration in the forearc mantle wedge. Geology 31, 525–528.

Hattori, K., Guillot, S., 2007. Geochemical character of serpentinites associated with high- to ultrahigh-pressure metamorphic rocks in the Alps, Cuba, and the Himalayas: recycling of elements in subduction zones. Geochemistry, Geophysics, Geosystems 8. http://dx.doi.org/10.1029/2007GC001594.

Ionov, D.A., Savoyant, L., Dupuy, C., 1992. Application of the ICP-MS technique to trace element analysis of peridotites and their minerals. Geostandards Newsletter 16 (2), 311–315.

Jagoutz, E., Palme, H., Baddenhausen, H., Blum, K., Cendales, M., Dreibus, G., Spettel, B., Lorenz, V., Vanke, H., 1979. The abundance of major, minor and trace elements in the Earth's mantle as derived from primitive ultramafic nodules. Geochimica et Cosmochimica Acta 11, 2031–2050.

Jochum, K.P., Stoll, B., 2008. Reference materials for elemental and isotopic analyses by LA-(MC)-ICP-MS: successes and outstanding needs. Mineralogical Association of Canada 40, 147–168.

Jochum, K.P., Willbold, M., Raczek, I., Stoll, B., Herwig, K., 2005. Chemical characterisation of the USGS reference glasses GSA-1G, GSC-1G, GSD-1G, GSE-1G, BCR-2G, BHVO-2G and BIR-1G Using EPMA, ID-TIMS, ID-ICP-MS and LA-ICP-MS. Geostandards and Geoanalytical Research 29, 285–302.

Kodolányi, J., Pettke, T., 2011. Loss of trace elements from serpentinites during fluid-assisted transformation of chrysotile to antigorite — an example from Guatemala. Chemical Geology 284, 351–362.

Kodolányi, J., Pettke, T., Spandler, C., Kamber, B.S., Gméling, K., 2012. Geochemistry of ocean floor and fore-arc serpentinites. Constraints on the ultramafic input to subduction zones. Journal of Petrology 53, 235–270.

Lardeaux, J.M., Schwartz, S., Tricart, P., Paul, A., Guillot, S., Béthoux, N., Masson, F., 2006. A crustal-scale cross-section of the south-western Alps combining geophysical and geological imagery. Terra Nova 18, 412–422.

Lemoine, M., Bourbon, M., de Graciansky, P.C., Letolle, R., 1983. Carbon and oxygen isotopes in limestones associated with ophiolites (western Alps, Corsica, Apennines) — possible indicators of a Tethyan oceanic hydrothermalism. Revue de Géologie Dynamique et de Géographie Physique 24, 305–314.

Lemoine, M., Marthaler, M., Caron, M., Sartori, M., Amaudric du Chaffaut, S., Dumont, T., Escher, A., Masson, H., Polino, R., Tricart, P., 1984. Discovery of Late Cretaceous planktonic Foraminifera in the Piemont Schistes Lustrés of the Queyras area (French Western Alps). Comptes Rendus de l'Académie des Sciences 299, 727–732.

Lemoine, M., Bas, T., Arnaud-Vanneau, A., Arnaud, H., Dumont, T., Gidon, M., Bourbon, M., de Graciansky, P.C., Rudkiewicz, J.L., Megard-Galli, J., Tricart, P., 1986. The continental margin of the Mesozoic Tethys in the Western Alps. Marine and Petroleum Geology 3, 179–199.

Lombardo, B., Nervo, R., Compagnoni, R., Messiga, B., Kienast, J.R., Mevel, C., Fiora, L., Piccardo, G.B., Lanza, R., 1978. Osservazioni preliminari sulle ofiolite metamorfiche del Monviso (Alpi occidentali). Rendiconti della Società Italiana di Mineralogia e Petrologia 34, 253–305.

Martin, B., Fyfe, W.S., 1970. Some experimental and theoretical observations on the kinetics of hydration reactions with particular reference to serpentinization. Chemical Geology 6, 185–202.

McDonough, W., Sun, S.S., 1995. The composition of the earth. Chemical Geology 120, 223–253.

Mével, C., 2003. Serpentinization of abyssal peridotites at mid-ocean ridges. Comptes Rendus Geosciences 335, 825–852.

Moody, J.B., 1976. Serpentinization: a review. Lithos 9, 125–138.

Pabst, S., Zack, T., Savov, I.P., Ludwig, T., Rost, D., Vicenzi, E.P., 2011. Evidence for boron incorporation into the serpentine crystal structure. American Mineralogist 96, 1112–1119.
Parkinson, I.J., Pearce, J.A., 1998. Peridotites from the Izu-Bonin-Mariana Forearc (ODP Leg 125): evidence for mantle melting and melt–mantle interaction in a supra-subduction zone setting. Journal of Petrology 39, 1577–1618.
Paulick, H., Bach, W., Godard, M., De Hoog, J.C.M., Suhr, G., Harvey, J., 2006. Geochemistry of abyssal peridotites (Mid-Atlantic Ridge, 15°20′N, ODP Leg 209): Implications for fluid/rock interaction in slow spreading environments. Chemical Geology 234, 179–210.
Peacock, S.M., 1990. Fluid processes in subduction zones. Science 258, 329–337.
Peacock, S.M., 1993. Large-scale hydration of the lithosphere above subducting slabs. Chemical Geology 108, 49–59.
Pearce, N.J.G., Perkins, W.T., Westgate, J.A., Gorton, M.P., Jackson, S.E., Neal, C.R., Chenery, S.P., 1997. A compilation of new and published major and trace element data for NIST SRM 610 and NIST SRM 612 glass reference materials. Geostandars Newsletter - The Journal of Geostandars and Geoanalysis 21, 115-114.
Rehkämper, M., Hofmann, A.W., 1997. Recycled ocean crust and sediment in Indian Ocean MORB. Earth and Planetary Science Letters 147, 93–106.
Rüpke, L.H., Morgan, J., Hort, M., Connolly, J.A., 2002. Are the regional variations in Central American arc lavas due to differing basaltic versus peridotitic slab sources of fluids? Geology 1035–1038.
Savov, I.P., Ryan, J.G., D'Antonio, M., Fryer, P., 2007. Shallow slab fluid release across and along the Mariana arc-basin system: insights from geochemistry of serpentinized peridotites from the Mariana fore arc. Journal of Geophysical Research 112, B09205. http://dx.doi.org/10.1029/2006JB004749.
Scambelluri, M., Philippot, P., 2001. Deep fluids in subduction zones. Lithos 55, 213–227.
Scambelluri, M., Bottazzi, P., Trommsdorff, V., Vannucci, R., Hermann, J., Gòmez-Pugnaire, M.T., Lòpez-Sànchez Vizcaino, V., 2001. Incompatible element-rich fluids released by antigorite breakdown in deeply subducted mantle. Earth and Planetary Science Letters 192, 457–470.
Scambelluri, M., Müntener, O., Ottolini, L., Pettke, T.T., Vannucci, R., 2004. The fate of B, Cl and Li in the subducted oceanic mantle and in the antigorite breakdown fluids. Earth and Planetary Science Letters 222, 217–234.
Schwartz, S., Lardeaux, J.M., Guillot, S., Tricart, P., 2000. The diversity of eclogitic metamorphism in the Monviso ophiolitic complex, western Alps, Italy. Geodinamica Acta 13, 169–188.
Schwartz, S., Allemand, P., Guillot, S., 2001. Numerical model of the effect of serpentinites on the exhumation of eclogitic rocks: insights from the Monviso ophiolitic massif (western Alps). Tectonophysics 342, 93–206.
Schwartz, S., Lardeaux, J.M., Tricart, P., Guillot, S., Labrin, E., 2007. Diachronous exhumation of HP–LT metamorphic rocks from south-western Alps: evidence from fission-track analysis. Terra Nova 19, 133–140.
Schwartz, S., Tricart, P., Lardeaux, J.M., Guillot, S., Vidal, O., 2009. Late tectonic and metamorphic evolution of the Piedmont accretionary wedge (Queyras Schistes lustrés, western Alps): evidences for tilting during Alpine collision. Geological Society of America Bulletin 121, 502–518.
Schwartz, S., Guillot, S., Reynard, B., Lafay, R., Nicollet, C., Debret, B., Auzende, A.L., 2013. Pressure–temperature estimates of the lizardite/antigorite transition in high pressure serpentinites. Lithos. http://dx.doi.org/10.1016/j.lithos.2012.11.023.
Seitz, M.G., Hart, S.R., 1973. Uranium and boron distributions in some oceanic ultramafic rocks. Earth and Planetary Science Letters 21, 97–107.
Seyfried, W.E., Foustoukos, D.I., Fu, Q., 2007. Redox evolution and mass transfer during serpentinization: An experimental and theoretical study at 200 °C, 500 bar with implications for ultramafic-hosted hydrothermal systems at Mid-Ocean Ridges. Geochimica et Cosmochimica Acta 71, 3872–3886.
Spandler, C., Pettke, T., Rubatto, D., 2011. Internal and external fluid sources for eclogite-facies veins in the Monviso meta-ophiolite, Western Alps: implications for fluid flow in subduction zones. Journal of Petrology 52 (6), 1207–1236.
Sun, M., Kerrich, R., 1995. Rare earth element and high field strength element characteristics of whole rocks and mineral separates of ultramafic nodules in Cenozoic volcanic vents of southeastern British Columbia, Canada. Geochimica et Cosmochimica Acta 59, 4863–4879.
Thompson, G., Melson, W.G., 1970. Boron contents of serpentinites and metabasalts in the oceanic crust: implications for the boron cycle in the oceans. Earth and Planetary Science Letters 8, 61–65.
Tricart, P., Lemoine, M., 1991. The Queyras ophiolite West of Monte Viso (Western Alps): indicator of a pecular ocean floor in the Mesozoic Tethys. Journal of Geodynamics 13, 163–181.
Tricart, P., Schwartz, S., 2006. A north–south section across the Queyras Schistes lustrés (Piedmont zone, Western Alps): syn-collision refolding of a subduction wedge. Eclogae Geologicae Helvetiae 99, 429–442.
Tricart, P., Schwartz, S., Sue, C., Lardeaux, J.M., 2004. Evidence of synextension tilting and doming during final exhumation from analysis of multistage faults (Queyras Schistes lustrés, Western Alps). Journal of Structural Geology 26, 1633–1645.
Ulmer, P., Trommsdorff, V., 1995. Serpentine stability to mantle depths and subduction-related magmatism. Science 268, 858–861.
Van Achterberg, E., Ryan, C., Jackson, S., Griffin, W., 2001. Data reduction software for LA-ICP-MS. In: Sylvester, P. (Ed.), Laser Ablation ICP-MS in the Earth Science. Mineralogical Association of Canada, pp. 239–243.
Vils, F., Pelletier, L., Kalt, A., Müntener, O., Ludwig, T., 2008. The lithium, boron and beryllium content of serpentinized peridotites from ODP Leg 209 (Sites 1272A and 1274A): implications for lithium and boron budgets of oceanic lithosphere. Geochimica et Cosmochimica Acta 72, 5475–5504.
Vils, F., Tonarini, S., Kalt, A., Seitz, H.M., 2009. Boron, lithium and strontium isotopes as tracers of seawater–serpentinite interaction at Mid-Atlantic ridge, ODP Leg 209. Earth and Planetary Science Letters 286, 414–425.
Vils, F., Müntener, O., Kalt, A., Ludwig, T., 2011. Implications of the serpentine phase transition on the behaviour of beryllium and lithium–boron of subducted ultramafic rocks. Geochimica et Cosmochimica Acta 75, 1249–1271.
Wicks, F.J., Whittaker, E.J.W., 1977. Serpentine textures and serpentinization. The Canadian Mineralogist 15, 459–488.
Wunder, B., Schreyer, W., 1997. Antigorite: high-pressure stability in the system MgO–SiO_2–H_2O (MSH). Lithos 41, 213–227.
Wunder, B., Wirth, R., Gottschalk, M., 2001. Antigorite: pressure and temperature dependence of polysomatism and water content. European Journal of Mineralogy 13, 485–495.
You, C.F., Gieskes, J.M., 2001. Hydrothermal alteration of hemi-pelagic sediments: experimental evaluation of geochemical processes in shallow subduction zones. Applied Geochemistry 16, 1055–1066.
You, C.F., Castillo, P.R., Gieskes, J.M., Chan, L.H., Spivack, A.J., 1996. Trace element behavior in hydrothermal experiments: implications for fluid processes at shallow depths in subduction zones. Earth and Planetary Science Letters 140, 41–52.